Nano Research

ISSN 1998-0124 CN 11-5974/O4
https://doi.org/10.26599/NR.2026.94909107

Research Article

Dynamic hydrogels with repeatable ultrasound-activated microbubble oscillation enable stepwise spatiotemporal growth factor release for tissue regeneration

Lili Ren[1], Jingyi Su[1], Yuxuan Chen[1], Zhixuan Wang[1], Li Min Tay[2], Wenjing Yang[1], Lixing Weng[1], Siyu Wang[1](✉), Chenjie Xu[3](✉), Lianhui Wang[1](✉), Yu Gao[1](✉)

[1] State Key Laboratory of Flexible Electronics (LoFE) & Jiangsu Key Laboratory of Smart Biomaterials and Theranostic Technology, Institute of Advanced Materials (IAM), Nanjing University of Posts & Telecommunications, Nanjing 210023, China

[2] School of Chemical and Biomedical Engineering, Nanyang Technological University, Singapore 639798, Singapore

[3] Department of Biomedical Engineering, College of Biomedicine, City University of Hong Kong, Kowloon Tong, Hong Kong 999077, China

Nano Res., **Just Accepted Manuscript** • https://doi.org/10.26599/NR.2026.94909107
https://www.sciopen.com/journal/1998-0124 on Aug. 11, 2026

TABLE OF CONTENTS (TOC)

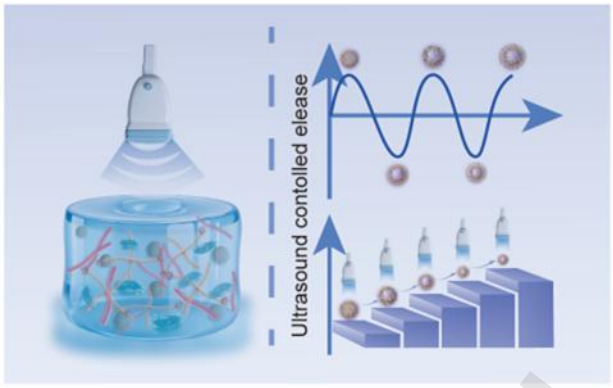

Ultrasound activates repeatable stable oscillation of engineered microbubbles within a dynamic hydrogel, enabling stepwise spatiotemporal controlled growth factor release while preserving scaffold integrity. This strategy provides precise therapeutic dosing for enhanced tissue regeneration.

Nano Research

Open Access

Research Article

Dynamic hydrogels with repeatable ultrasound-activated microbubble oscillation enable stepwise spatiotemporal growth factor release for tissue regeneration

Lili Ren[1], Jingyi Su[1], Yuxuan Chen[1], Zhixuan Wang[1], Li Min Tay[2], Wenjing Yang[1], Lixing Weng[1], Siyu Wang [1] ✉, Chenjie Xu [3] ✉, Lianhui Wang [1] ✉, and Yu Gao [1] ✉

[1]*State Key Laboratory of Flexible Electronics (LoFE) & Jiangsu Key Laboratory of Smart Biomaterials and Theranostic Technology, Institute of Advanced Materials (IAM), Nanjing University of Posts & Telecommunications, Nanjing 210023, China*
[2]*School of Chemical and Biomedical Engineering, Nanyang Technological University, Singapore 639798, Singapore*
[3]*Department of Biomedical Engineering, College of Biomedicine, City University of Hong Kong, Kowloon Tong, Hong Kong 999077, China*

Received: 1 June 2026; **Revised:** 6 August 2026; **Accepted:**11 August 2026

✉Address correspondence to Yu Gao, iamygao@njupt.edu.cn; Lianhui Wang, iamlhwang@njupt.edu.cn; Chenjie Xu, chenjie.xu@cityu.edu.hk; Siyu Wang, amsiyuwang@njupt.edu.cn

Cite this article: *Nano Research*, 2026, 19, 94909107 https://doi.org/10.26599/NR.2026.94909107

ABSTRACT: Effective tissue regeneration requires precise spatiotemporal therapeutic delivery while maintaining scaffold mechanical integrity, which remains a major challenge in regenerative medicine. Here, we present an ultrasound (US)-activated tissue regeneration platform based on engineered osteogenic microbubbles (MMB-BMPs) embedded in a dynamic hyaluronic acid hydrogel (dHA), forming a mechanically robust scaffold (dHAMBH). Upon repeated US stimulation at the resonant frequency, MMB-BMPs underwent stable oscillation within the hydrogel, enabling stepwise, on-demand release of iron oxide nanoparticles (IONPs) and bone morphogenetic protein-2 (BMP-2), while maintaining scaffold integrity after multiple stimulations cycles. This controlled co-delivery enhances osteogenic differentiation of human bone marrow-derived mesenchymal stromal cells (hMSCs). In a mouse critical-sized calvarial defect model, the dHAMBH hydrogel combined with US stimulation accelerated bone regeneration, achieving a 1.7-fold increase in new bone volume compared with the non-US stimulated control. Overall, this work establishes a US-activated platform that enables precise, repeatable therapeutic delivery to enhance tissue regeneration.

KEYWORDS: ultrasound stimulation; controlled drug delivery; microbubbles; stable oscillation; tissue regeneration

1 Introduction

Tissue and organ damage caused by trauma, chronic disease, or aging is increasingly prevalent and poses significant challenges for effective clinical repair [1,2]. Scaffolds incorporating stem cells and osteoinductive factors, such as bone morphogenetic protein-2 (BMP-2), have emerged as a promising strategy for promoting the osteogenic differentiation of human bone marrow-derived mesenchymal stromal cells (hMSCs) and accelerating new bone formation [3,4]. Successful regeneration relies on the precise spatiotemporal control of therapeutic agent release at the injury site. This helps to maintain optimal local concentrations, regulate cell signaling and minimize systemic side effects [5,6]. However, achieving controlled release while preserving the mechanical strength and structural integrity remains a major obstacle in developing functional tissue engineering platforms.

Ultrasound (US) has emerged as a powerful external stimulus for drug delivery due to its noninvasive nature, deep tissue penetration, and precise spatiotemporal controllability, and it has been widely adopted in clinical applications [7]. In particular, when combined with microbubbles (MBs), US can induce MBs cavitation, whereby MBs expansion and collapse trigger payload release at target sites. However, cavitation-driven release is typically rapid and poorly controlled, limiting the precise, repeatable, and sustained delivery required for tissue regeneration. US-responsive acoustic nanodroplets, typically comprising a liquid perfluorocarbon core surrounded by a lipid, polymer, or protein shell, can enable localized and on-demand drug release through acoustic droplet vaporization (ADV) process, the release behavior depends on the liquid-to-gas phase transition and the subsequent dynamics of the vaporized bubbles, which may include expansion, cavitation, or rupture. Moreover, the vaporization threshold and post-vaporization behavior are influenced by the perfluorocarbon composition, droplet size, temperature, and US parameters, thereby limit precise control over the drug-release profile [8,9]. Our previous work demonstrated that precision-engineered self-assembled nanoparticle-shelled microbubbles (MMBs) exhibit stable oscillatory behavior and controlled release when activated by US at their resonant frequencies in aqueous environments, thereby avoiding cavitation-induced

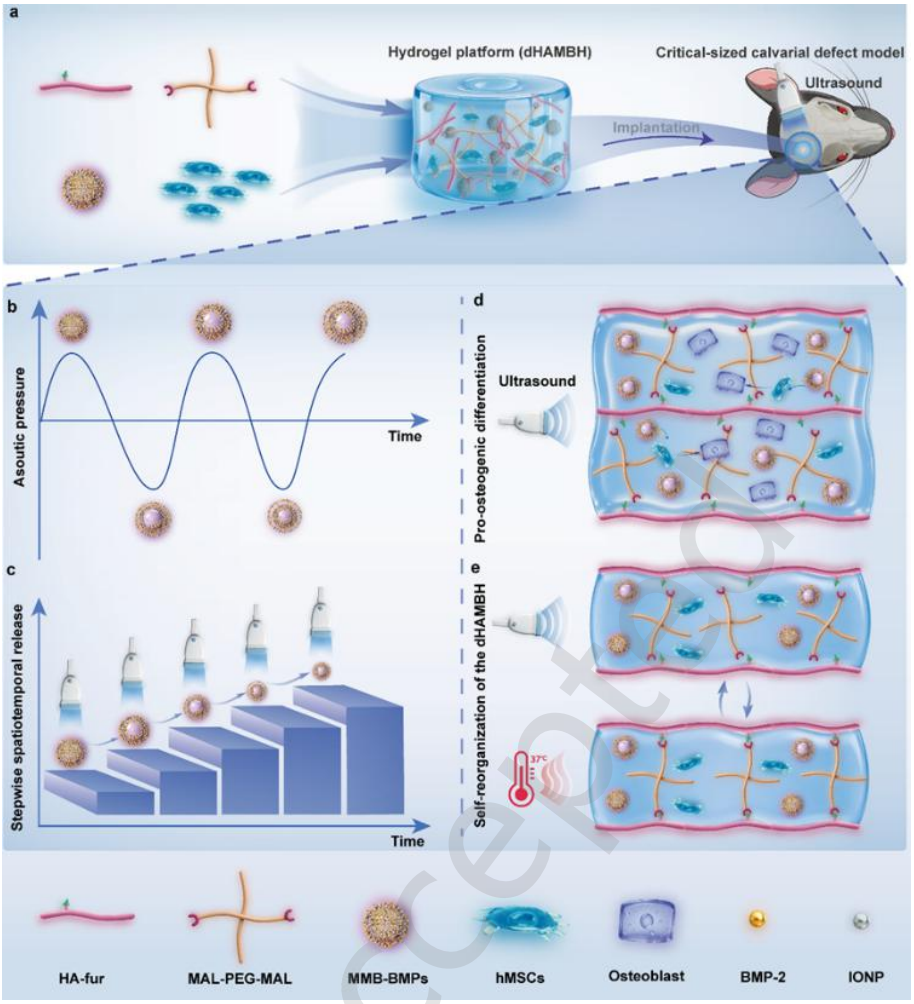

Figure 1 Schematic illustration of an ultrasound (US)-activated dynamic hydrogel platform (dHAMBH) for spatiotemporally controlled drug release in bone tissue regeneration. (a) Fabrication of the dHAMBH hydrogel by co-encapsulating MMB-BMPs and hMSCs within the dHA hydrogel followed by implantation into a mouse calvarial critical-sized defect model. (b) Under US activation, MMB-BMPs undergo stable oscillation and enable controlled release of IONPs and BMP-2 within the dHAMBH hydrogel. (c) Repeated US stimulation induces stepwise release of therapeutic cargos from MMB-BMPs within the dHAMBH hydrogel. (d) US-triggered release of IONPs and BMP-2 within the dHAMBH hydrogel synergistically promote the osteogenic differentiation of hMSCs. (e) Self-reorganization behavior of the dHAMBH hydrogel under physiological conditions after repeated US stimulation, where dynamic covalent Diels-Alder (D-A) linkages enable reversible network reformation and preservation of hydrogel structural integrity.

burst release [10,11]. For regenerative applications, such controlled release must be integrated within a scaffold capable of localizing therapeutic cargos, supporting cell viability, and providing an appropriate three-dimensional (3D) microenvironment. Hydrogels are promising candidates due to their high water content, excellent biocompatibility, and tunable mechanical properties [12]. For example, hydrogels incorporating hMSCs have demonstrated significant potential for tissue regeneration [13,14]. Nevertheless, exposure to US may disrupt the hydrogel network, reduce stiffness and elasticity, or increase brittleness, thereby compromising the structural integrity and mechanical stability of the scaffold. Therefore, achieving controlled US-mediated drug release within hydrogels without compromising hydrogel network integrity remains a significant challenge, limiting precise in situ control of therapeutic dosing.

Dynamic cross-linked hydrogels have gained increasing attention for tissue regeneration, owing to their highly hydrated polymeric networks and meshes like structures [15-18]. Unlike static chemically cross-linked hydrogels, dynamic hydrogels contain reversible chemical or physical bonds, which can adapt to local mechanical forces or biological signals, enabling the autonomous reconfiguration of the network after structural damage [19]. Their extracellular matrix-mimicking architecture provides a favorable microenvironment for cell attachment and migration. In addition, these dynamic networks can preserve structural integrity and mechanical strength after deformation induced by external stimuli [20, 21], making them as attractive scaffolds for tissue regeneration.

Building on these findings, we hypothesized that engineered MMBs could be activated by US at their resonant frequencies and undergo stable oscillation within a dynamic hydrogel, thereby enabling controlled drug release and promoting tissue regeneration. To test this hypothesis, we developed osteogenic nanoparticle-shelled microbubbles (MMB-BMPs) via the self-assembly of iron oxide nanoparticles (IONPs) and BMP-2, at the liquid-air interface. MMB-BMPs and hMSCs were co-encapsulated within a dynamic hyaluronic acid (dHA) hydrogel formed by Diels-Alder (D-A) click crosslinking between furan-modified hyaluronic acid (HA-furan) and maleimide-polyethylene glycol-maleimide (MAL-PEG-MAL). The resulting composite

hydrogel platform (dHAMBH) was then implanted into a mouse critical-sized calvarial defect model (Fig. 1(a)). Upon repeated US stimulation, MMB-BMPs exhibited stable oscillation, triggering controlled and stepwise release of IONPs and BMP-2, thereby synergistically promoting the osteogenic differentiation of hMSCs within the hydrogel at the defect site. Meanwhile, the presence of reversible covalent bonds endowed the hydrogel with self-reorganization capability at physiological temperature (37°C), preserving MMB-BMPs integrity, supporting hMSCs viability and proliferation, and maintaining a stable 3D microenvironment, ultimately facilitating tissue regeneration (Figs. 1(b)-1(e)).

2 Experimental

2.1 Preparation and characterization of MMB-BMPs

The MMB-BMPs were prepared following a previously reported method with minor modifications [10, 11]. A mixture containing BMP-2 solution (1 mg mL^{-1}, 150 μL), SDS solution (10 mM, 150 μL), and IONP solution (10 mg mL^{-1}, 400 μL) was homogenized at 20,000 rpm for 3 minutes. The resulting MMB-BMPs were allowed to stabilize overnight to facilitate close packing of the IONP shell. Finally, the MMB-BMPs were magnetically separated and washed three times with deionized water. The morphology of MMB-BMPs was observed using an optical microscope (Olympus IX71, Japan) and scanning electron microscope (Hitachi S4800, Japan). Diameters were determined from the acquired images by measuring at least 100 individual MMBs. The fluorescent images of MMBs were obtained by the laser scanning confocal microscope (Olympus FV1000MPE, Japan). The iron (Fe) content was quantified using inductively coupled plasma optical emission spectrometry (ICP-OES, PerkinElmer, USA). The content of BMP-2 was measured using a human BMP-2 ELISA kit (KeyGen, China).

2.2 Synthesis and characterization of HA-furan and dHA

Furan-modified hyaluronic acid (HA-furan) and dHA hydrogels were synthesized based on previously reported protocols [22]. Briefly, HA (2.5 mmol) was dissolved in 100 mL of MES buffer (100 mM, pH 5.5). To activate the carboxyl groups, DMTMM (5 mmol) was added and the solution was stirred for 20 minutes. Furylamine (2.5 mmol) was then added dropwise, and the reaction mixture was stirred at room temperature for 24 hours. The resulting product was dialyzed for 72 hours using a dialysis membrane with a molecular weight cutoff (MWCO) of 14 kDa, followed by freeze-drying for further use. ^{1}H NMR spectra of the HA-furan conjugate were recorded using a Bruker Avance Neo 400 MHz spectrometer. To prepare the dHA hydrogels, HA-furan was dissolved in phosphate-buffered saline (PBS) at various concentrations (10, 15, 20, and 50 mg mL^{-1}). The solution was then mixed with MAL-PEG-MAL crosslinker at a 1:1 molar ratio of furan to maleimide groups to form a dHA hydrogel network through D-A click chemistry.

The dynamic cross-linked properties of the dHA hydrogel were assessed by subjecting the samples to US stimulation (400-800 kHz, 0.5 W cm^{-2}), followed by incubation in a container at 37°C for 4 hours. Compressive stress-strain curves were measured using an Electromechanical Universal Testing Machine (CMT6502, MTS, China) equipped with a 10 N static load cell and Power Test software. Cylindrical hydrogel samples (diameter: 12 mm; height: 5 mm) were compressed between two parallel plates at a crosshead speed of 1 mm min^{-1} until maximum strain was reached. The compressive modulus was calculated from the linear region of the stress-strain curve.

2.3 US induces stable oscillations of MMBs in solution

To evaluate US-triggered release in solution, HSA was used in place of BMP-2. US frequencies ranging from 400 to 800 kHz with an amplitude of 20 Vpp were generated using a function generator (Keysight, USA). Acoustic intensities of 0.1, 0.3, 0.5, and 1.0 W cm^{-2} were applied.. Each US cycle consisted of 4 seconds of exposure followed by a 1 second pause. After exposure to varying numbers of cycles, the amount of HSA released from the MMBs was quantified using a BCA protein assay kit (KeyGen, China), according to the manufacturer's instructions.

2.4 US induces stable oscillations of MMBs in hydrogel

MMBs were embedded in 0.75% and 1.5% (W/V) agarose solutions before gelation. US parameters were consistent with those used in the solution-based experiments. The stable oscillation behavior of MMBs during US exposure was recorded using an ultrahigh-speed camera, and changes in MMBs diameter were quantified from the captured video frames. To assess US-triggered drug release from hydrogels, rhodamine-labeled HSA loaded MMBs were incorporated into the dHA precursor solution and allowed to gel at 37°C for 2 hours via D-A crosslinking. US was applied at varying cycle durations every 24 hours over a total period of 168 hours. After each US exposure, the hydrogels were incubated at 37°C for 2 hours, and the release medium was subsequently collected. The amount of HSA released was quantified by measuring fluorescence intensity using a fluorescence spectrophotometer based on the standard curve. Additionally, the spatial distribution and structural integrity of MMB-HSA before and after US stimulation were visualized using 2D and 3D imaging via laser scanning confocal microscopy.

2.5 Cell culture

Human bone marrow mesenchymal stromal cells (hMSCs, HUXMA-01001, Cyagen) were cultured in Dulbecco's Modified Eagle Medium (DMEM; Gibco, USA) supplemented with 10% fetal bovine serum (FBS; Gibco, USA) and 1% penicillin-streptomycin (P/S; Gibco, USA). Cells were maintained under standard culture conditions at 37°C containing 5% CO_2. The culture medium was refreshed every 3 days. For all experiments, hMSCs at passages 4 to 6 were used.

2.6 hMSCs culture on and within dHA hydrogels

All materials were sterilized by autoclaving at 121°C for 20 minutes prior to cell seeding. hMSCs were used at a concentration of 1 × 10^6 cells mL^{-1}. For culture on the surface of dHA, 50 μL of hydrogel precursor solution was added to 96-well plate and allowed to gel at 37°C. After complete gelation, 100 μL of hMSCs suspension was evenly added on top of the hydrogel surface. For encapsulation within dHA, the hMSCs suspension was mixed directly with the hydrogel precursor solution, followed by incubation at 37°C for 2 hours to allow in situ gelation and cell encapsulation.

Cell viability was assessed using a Live/Dead Cell Kit

(KeyGen, China) following the manufacturer's protocol. CLSM was used to visualize stained cells at days 1, 7, and 14. To assess cell proliferation, the double-stranded DNA (dsDNA) content was quantified using a PicoGreen dsDNA Quantification Kit (Invitrogen, USA). At days 1, 7, and 14, dHA hydrogels encapsulating hMSCs were washed three times with PBS and stored at -80°C until analysis. Before quantification, samples were thawed and homogenized in 1 mL of MES buffer using a tissue homogenizer to lyse the cell membranes. Subsequently, 100 μL of the homogenized solution was mixed with 100 μL of PicoGreen reagent and incubated in the dark at room temperature for 3 minutes. Fluorescence intensity was measured using a microplate reader (excitation: 480 nm, emission: 520 nm), and DNA concentrations were calculated based on a standard curve.

2.7 Alizarin red staining

hMSCs were seeded in 6-well plates and cultured in osteogenic differentiation medium composed of low-glucose DMEM supplemented with 10% FBS, 100 U mL^{-1} P/S, 10 nM dexamethasone, 10 mM β-glycerophosphate, and 0.05 mM ascorbic acid-2-phosphate. Cells were treated with PBS (control), IONPs (50 μg mL^{-1}), BMP-2 (25 ng mL^{-1}), or MMB-BMPs containing an equivalent amount of BMP-2, and cultured for 14, 18, and 21 days. After treatment, cells were fixed with 4% paraformaldehyde (PFA) for 20 minutes and washed three times with calcium- and magnesium-free PBS. Alizarin red staining was then performed using a commercial Osteogenesis Staining Kit (Beyotime, China) following the manufacturer's instructions. The staining solution was applied to cover the cells completely and incubated at room temperature for 30 minutes. After thorough washing with distilled water to remove excess dye, and observed using an inverted microscope (Olympus IX71, Japan).

2.8 Western blot analysis

For Western blot analysis of Smad1/5/8 and p38 MAPK, cells were seeded at a density of 1×10^6 per dish and cultured in serum-free medium overnight for starvation. Following starvation, the cells were treated with IONPs (50 μg mL^{-1}) and BMP-2 (25 ng mL^{-1}) for 1 hour. After treatment, cells were lysed on ice using RIPA lysis buffer (P0013C, Beyotime) freshly supplemented with protease and phosphatase inhibitor cocktail (P1045, Beyotime). The lysates were centrifuged at 12,000 rpm for 20 minute at 4°C, and the resulting supernatants were collected and stored at -20°C. Protein concentrations were determined using the BCA assay. Equal amounts of protein were separated by SDS-PAGE and transferred onto nitrocellulose membranes. After blocking with a protein-free rapid blocking buffer (G2052, Servicebio), the membranes were incubated with primary antibodies (K026147P, Solarbio; K000093M, Solarbio) diluted in TBST overnight at 4°C, followed by incubation with secondary HRP-linked antibodies (SA00001-2, proteintech) for 1 hour at room temperature. Protein bands were visualized using chemiluminescent substrate (BL523B, biosharp) and captured with the Tanon-5200 imaging system.

2.9 *In vitro* cell osteogenic differentiation

HA hydrogels encapsulating different components were prepared and divided into five groups: dHAH, dHABH (containing BMP-2 25 ng mL^{-1}), dHAM (containing IONPs 50 μg mL^{-1}), dHAMBH (containing both BMP-2 and IONPs), and dHAMBH combined with US stimulation (400-800 kHz, 0.5 W cm^{-2}). Before gelation, the hydrogel solutions were added to the upper chambers of Transwell inserts, with complete DMEM added to the lower chambers. The mixtures were then incubated at 37°C for 2 hours to allow gelation. After 14 days of culture, ALP activity was assessed using an Alkaline Phosphatase Assay Kit (Beyotime, China). Briefly, samples from each group were lysed using cell lysis buffer (Beyotime, China), then homogenized and centrifuged to obtain the supernatants. A colorimetric substrate was subsequently added, and the absorbance was measured at 405 nm using a microplate reader, following the manufacturer's protocol.

2.10 *In vivo* mice calvarial defect model

A critical sized calvarial defect model was established based on previously reported protocols [23]. C57BL/6J mice (8 weeks old, male) were anesthetized via isoflurane. The surgical area was shaved and disinfected with iodophor. After dissection of the periosteum, a full-thickness circular defect (4 mm in diameter) was created in the left parietal bone using a surgical drilling and trephine. The defect was then filled with the following hydrogels: dHAH, dHABH (containing BMP-2 200 ng), dHAM (containing IONPs 32 μg), or dHAMBH (containing both BMP-2 and IONPs). The incision was sutured following implantation. After surgery, the mice were placed on a heating pad for recovery and given free access to food and water. For the dHAMBH hydrogel treated group, US stimulation (400-800 kHz, 0.5 W cm^{-2}) was applied every other day during the first two weeks post-implantation. Bone regeneration at the defect site was monitored at 6-, 8- and 10-weeks post-implantation using NEMO Micro-computed Tomography (NMC-200) at two-week intervals. Scanning was performed with a voltage of 90 kV, a current of 200 μA, and a resolution of 2 μm. The projection images were reconstructed into three-dimensional models using Hiscan Analyzer software to evaluate osteogenesis. The Analysis-0810 software was used to conduct an analysis of regions of interest (ROIs), which included areas of newly formed bone and defect areas. Quantitative parameters, including bone volume (BV, mm^3) and trabecular separation

3 Results and discussion

3.1 Preparation and characterization of MMB-BMPs

To prepare the MMB-BMPs, a mixture of BMP-2, IONPs, and sodium dodecyl sulfate (SDS) was homogenized. During this process, IONPs rapidly self-assembled at the liquid-air interface, forming a dense shell structure (Fig. S1). Simultaneously, BMP-2 was encapsulated within the interstitial spaces of the IONP shell to form MMB-BMPs. The resulting MMB-BMPs exhibited a uniform spherical morphology (Fig. 2(a)) with an average diameter of 7.55 ± 3.9 μm (Fig. 2(b)). To verify protein loading, rhodamine-labeled human serum albumin (HSA) was replaced with BMP-2. Confocal laser scanning microscopy (CLSM) revealed that there is a uniform green fluorescence signal surrounding the MMBs, confirming the successful loading of protein within the IONP shell layer (Fig. 2(c)). Notably, this loading strategy is not limited to proteins, small molecule

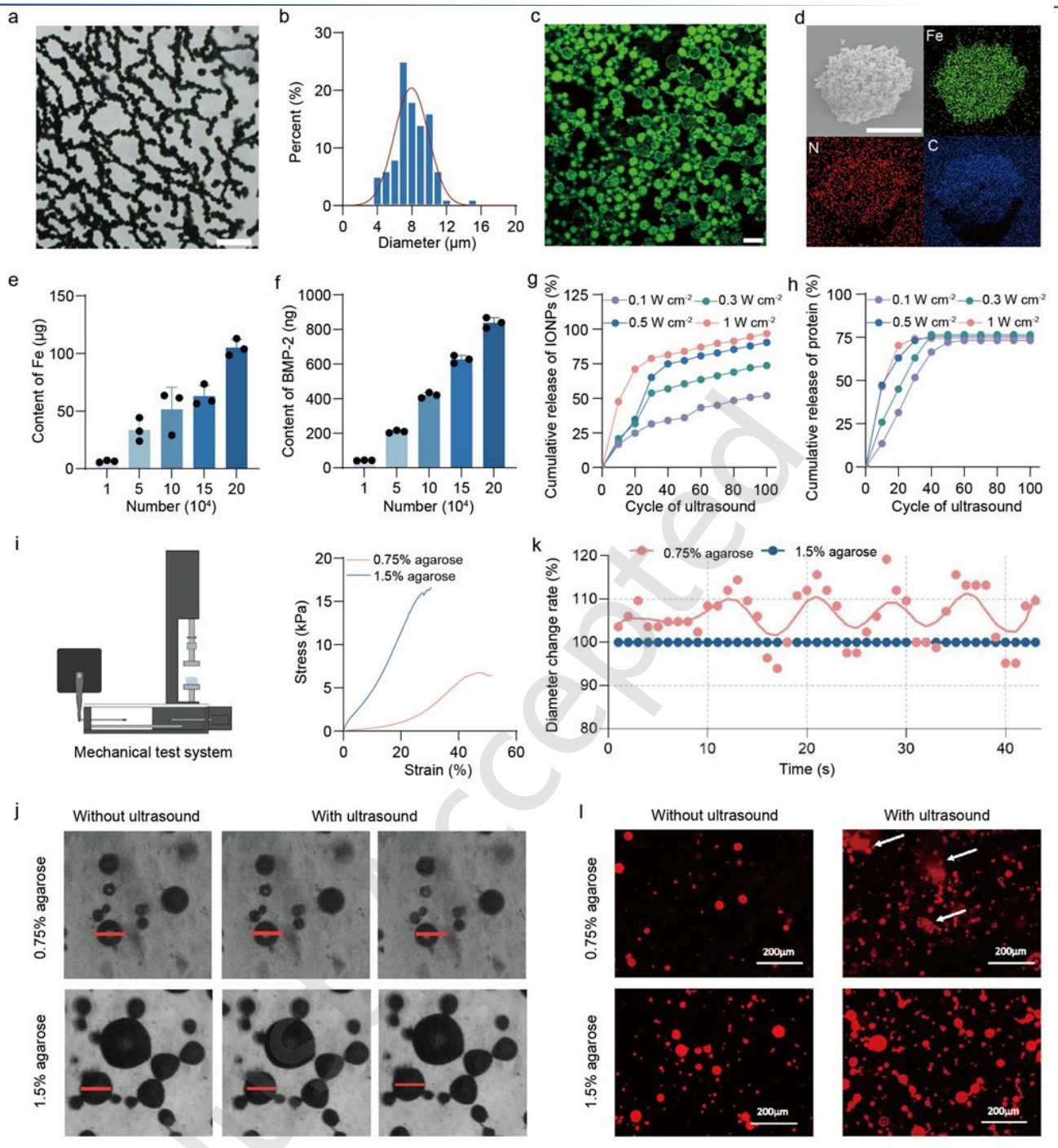

Figure 2 Preparation and characterization of MMB-BMPs. (a) Representative optical microscopy image of MMB-BMPs, Scale bar: 50 μm. (b) Diameter distribution of MMB-BMPs, n = 100. (c) Representative CLSM image of MMBs loaded with rhodamine-labeled HSA, Scale bar: 50 μm. (d) Representative SEM element mappings of a single MMB-BMP, Scale bar: 10 μm. (e) Quantification of Fe content in varying numbers of MMB-BMPs, n = 3. (f) Quantification of BMP-2 content in varying numbers of MMB-BMPs, n = 3. (g) Cumulative release profiles of IONPs from MMB-BMPs at differen US intensities. (h) Cumulative release profiles of protein from MMB-BMPs at different US intensities. (i) Schematic illustration of the mechanica testing setup (left) and compression stress-strain curves of different concentration agarose hydrogels (right). (j) Representative optical images o MMB oscillation in different concentration agarose hydrogels without or with US stimulation. Red lines indicate equivalent lengths. (k) Relative diameter changes of individual MMB in different concentration agarose hydrogels after US stimulation. (l) Representative fluorescence images o polystyrene microspheres released from MMBs in different concentration agarose hydrogels without or with US stimulation. White arrows indicate microsphere dispersion following US stimulation, Scale bars: 200 μm. Data were expressed as the mean ± SD.

drugs and other functional NPs can also be effectively loaded within the shell structure of multi-layered IONP shells (Fig. S2). Scanning electron microscope (SEM) elemental mapping analysis confirmed the presence and distribution of Fe, N, and C elements within the MMB-BMPs. This further validates the loading of both IONPs and BMP-2 (Fig. 2(d)). After counting the number of MMB-BMPs in different solution volumes (Fig. S3), the Fe content was quantified by inductively coupled plasma optical emission spectrometry (ICP-OES), and BMP-2 content was measured using an ELISA kit. The results showed that MMB-BMP contained approximately 8.47 μg mg^{-1} of Fe and 52.6 ng mg^{-1} of BMP-2, respectively (Figs. 2(e) and 2(f)).

Sustained and localized BMP-2 release is essential for promoting osteogenic differentiation, enhancing therapeutic efficacy, and minimizing undesired side effects. In this study, the engineered MMB-BMPs enabled controlled release of both IONPs and protein in a liquid environment through

stable oscillations under US stimulation at intensities below their cavitation threshold (Figs. 2(g) and 2(h)). Given that hydrogels are polymer networks with high water content, we hypothesized that MMB-BMPs could also achieve controlled release within hydrogels, which possess appropriate mechanical properties. To test this hypothesis, we first evaluated the stable oscillations of MMBs within agarose hydrogels. As shown in Fig. 2(i), MMBs were embedded in agarose hydrogels at concentrations of 0.75% and 1.5% (W/V), with their compression modulus determined by compression testing to be 13.79 kPa and 56.34 kPa, respectively. Under US stimulation at their resonant frequencies, MMBs exhibited stable oscillation behavior without collapsing in 0.75% agarose hydrogels (Fig. 2(j), Supplementary Movie 1). However, increasing the agarose concentration to 1.5% was found to limit the oscillation behavior of MMBs (Fig. 2(j), Supplementary Movie 2). Quantitative analysis of diameter changes under US stimulation revealed that MMBs in 0.75% agarose displayed time-dependent size variations due to oscillation, whereas those in 1.5% agarose showed no significant diameter change (Fig. 2(k)). To further evaluate drug release from hydrogels driven by stable oscillations, fluorescently labeled polystyrene microspheres were loaded into MMBs and embedded into agarose hydrogels. Fluorescence imaging showed that without US stimulation, no release of polystyrene microspheres was observed in either concentration of agarose hydrogel (Fig. 2(l)). In contrast, upon US stimulation, distinct fluorescent signals were detected surrounding MMBs embedded in 0.75% agarose hydrogel, indicating successful controlled release. However, no detectable diffusion of the fluorescence signal was observed in the 1.5% agarose hydrogel (Fig. 2(l)). These results suggested that the MMBs can undergo stable oscillation within hydrogels with an appropriate compression modulus. Based on this observation, US-induced stable oscillations of MMB-BMPs offer a promising strategy for achieving precisely controllable drug release within hydrogel matrices.

3.2 Preparation and characterization of the dHAMBH hydrogel

Agarose hydrogels lack the ability to recover after US stimulation, making them unsuitable as scaffolds for sustained localized drug delivery and cell adhesion. HA-based hydrogels have been extensively engineered for tissue repair due to their excellent biocompatibility and biodegradability. Here, we constructed a dHA hydrogel by crosslinking HA-furan with MAL-PEG-MAL through a D-A reaction (Fig. S4). Then, MMB-BMPs and hMSCs were also loaded into the hydrogel, forming a dHAMBH hydrogel (Fig. 3(a)). The dHAMBH hydrogel demonstrates biocompatibility and mechanical strength under physiological conditions, supporting hMSCs adhesion and proliferation. Moreover, the presence of reversible covalent bond enables rapid reorganization of the hydrogel architecture after repeated US stimulation, allowing it to maintain its mechanical properties following incubation at 37°C (Fig. 3(a)). The synthesis of HA-furan and the formation of the dHA hydrogel were confirmed by ^{1}H NMR and FTIR spectroscopy (Figs. S5 and S6). Quantitative analysis showed a significant reduction in pore size, confirming that a stable 3D dense network structure after the D-A reaction (Fig. S7). The dHA hydrogel was prepared using HA-furan at various concentrations (10, 15, 20, and 50 mg mL^{-1}) to optimize the mechanical properties for US-induced stable oscillations of MMBs (Fig. S8). Among these, the hydrogel prepared by 15 mg mL^{-1} of HA-furan exhibited mechanical strength comparable to that of 0.75% agarose and was selected for all *in vitro* and *in vivo* evaluations. Additionally, the dHA hydrogel showed excellent injectability and shape adaptability. After extrusion and remodeling into star and leaf shaped structures, it can still maintain structural integrity (Fig. S9). Subsequently, we assessed the reorganization behavior of the polymeric network within the dHA hydrogel in response to US stimulation. SEM imaging revealed that the mesopores of the hydrogel enlarged after US stimulation. However, after incubation at 37°C for a period of time, the mesopore size decreased and the interconnected polymeric network was restored, demonstrating the reorganization capability of the dHA hydrogel (Figs. 3(b)-3(d)). Consistently, after US stimulation, the stress of dHA hydrogel decreased to 3.4 kPa and recovered to 7.8 kPa following incubation at 37°C (Fig. 3(e)). The differential scanning calorimetry (DSC) results further confirmed the reversible behavior of the dHA hydrogel under physiological conditions (Fig. S10). These results demonstrate that the dHA hydrogel possesses dynamic network reorganization capability and can maintain structural integrity under physiological conditions even after US-induced disruption.

We further investigated whether US stimulation could activate stable oscillation of MMB-BMPs within the dHA hydrogel, thereby enabling controlled release. For visualization, rhodamine-labeled HSA was used in place of BMP-2 and loaded into MMBs, which were then embedded in the dHA hydrogel. To better mimic *in vivo* acoustic penetration conditions, particularly those relevant to the calvarial defect model, all US stimulation experiments were conducted with a layer of porcine skin placed between the transducer and the hydrogel scaffold. CLSM imaging confirmed that the MMBs were successfully and uniformly embedded within the hydrogel (Fig. S11). Subsequently, two-dimensional (2D) and 3D CLSM imaging showed that the fluorescent signal remained confined within the MMBs, with no observable diffusion into the hydrogel without US stimulation (Fig. 3(f)). In contrast, upon US stimulation at the resonant frequency, fluorescent molecules were gradually released from the MMBs' surface and diffused into the surrounding hydrogel, while the overall structure of the MMBs remained intact (Figs. 3(g) and S12). Quantitative analysis of cumulative protein release demonstrated that stable oscillation of MMB-BMPs under US stimulation at the resonant frequency enabled a stepwise and sustained release profile in the dHA hydrogel. Under repeated US stimulation every 24 hours over a 168 hours period, protein release increased rapidly during each US exposure and nearly ceased when the US was turned off, with minimal release observed during the off periods (Fig. 3(h)). After 7 days, cumulative protein release reached approximately 33% with 50 US cycles per stimulation and 74% with 100 cycles, demonstrating a stepwise and sustained US-

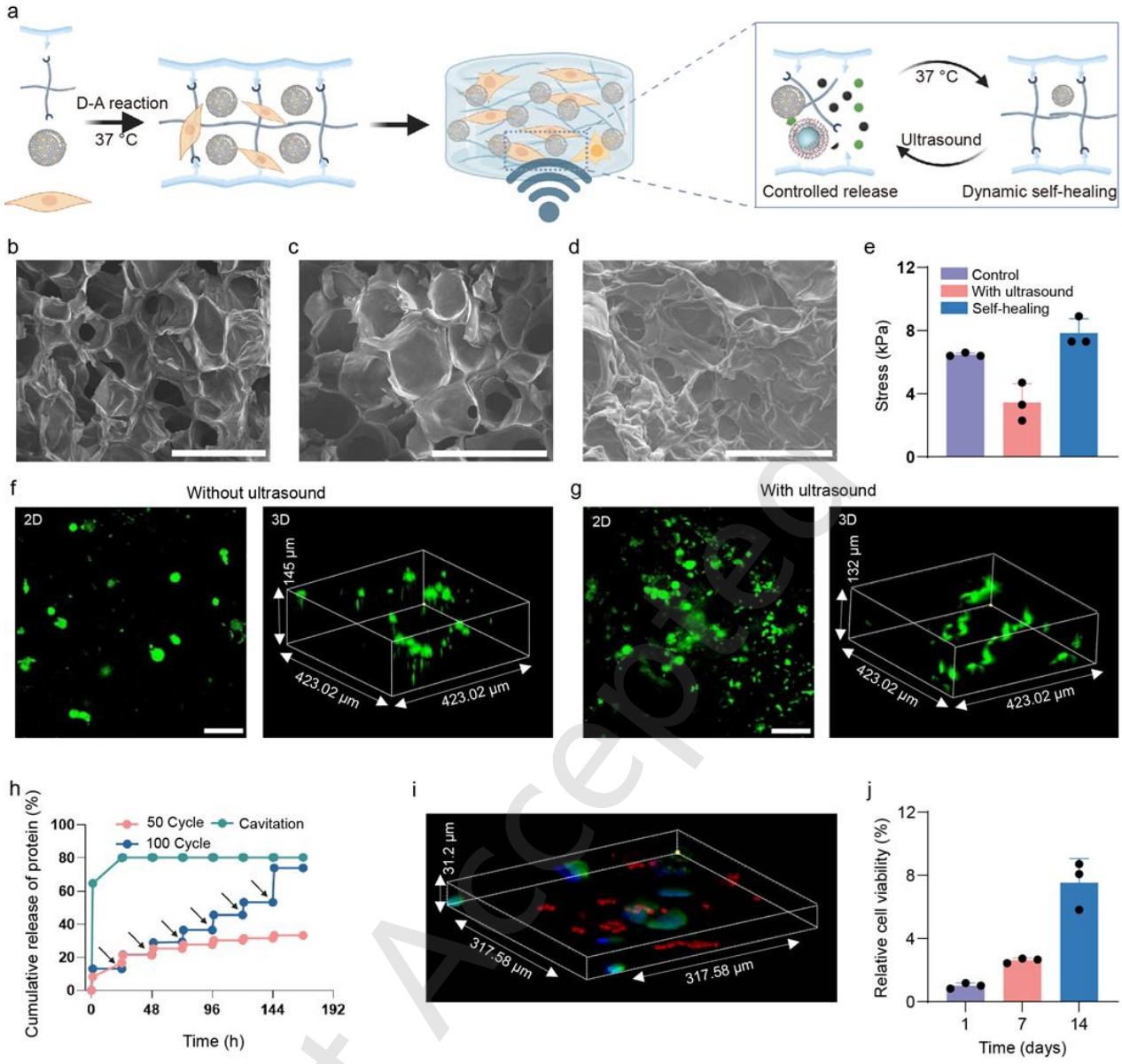

Figure 3 Preparation and characterization of the dHAMBH hydrogel. (a) Schematic illustration of the synthesis and self-reorganizatior mechanism of the dHAMBH hydrogel. (b) Representative SEM image of the dHA hydrogel. Scale bar: 300 μm. (c) Representative SEM image of the dH/ hydrogel after US stimulation. Scale bar: 300 μm. (d) Representative SEM image of the dHA hydrogel following incubation at 37°C. Scale bar: 200 μm (e) Quantification of stress in the dHA hydrogel before US, after US, and after incubation at 37°C, n = 3. Representative 2D and 3D CLSM images o rhodamine labelled MMBs in the dHA hydrogel without (f) and with (g) US stimulation. (h) Cumulative protein release profiles from the dHA hydroge under repeated US stimulation. Black arrows indicate US stimulation. (i) Representative 3D CLSM image of the dHAMBH hydrogel, blue: cell nucleus green: cytoplasm, red: MMBs. (j) Quantification of hMSCs proliferation within the dHAMBH hydrogel after 14 days. All data were expressed as the mean ± SD.

responsive release profile in the dHA hydrogel (Fig. 3(h)). In contrast, when the US intensity exceeded the threshold and triggered cavitation, more than 70% of the protein was released during a single stimulation, indicating burst release rather than controlled stepwise release (Fig. 3(h)). Furthermore, both US intensity and duration were found to influence the amount of protein released (Fig. S13). Increasing the US intensity from 0.1 W cm^{-2} to 1 W cm^{-2} resulted in a 15% increase in cumulative release over 7 days. Additionally, adjusting the HA hydrogel concentration (HA-furan) also altered the release profiles (Fig. S13). After US induced cargo release, the hydrogel retained mechanical strength, indicating that the hydrogel maintained its overall structural and mechanical integrity throughout the release process (Fig. S14). These results demonstrate that controlled drug release within the hydrogel can be achieved by inducing stable oscillation of MMBs at their resonant frequencies, thereby avoiding cavitation associated burst release. Moreover, the release behavior can be precisely regulated in practical applications by tuning US parameters and hydrogel properties.

We further evaluated the effect of the dHA hydrogel on hMSCs viability and proliferation. Live/dead imaging showed that hMSCs cultured on the surface of the dHA hydrogel maintained high viability and continuous proliferation over 14 days, with minimal cytotoxicity (Fig. S15). Subsequently, hMSCs were loaded within the dHA hydrogel (dHAH), where they remained uniformly distributed and exhibited sustained proliferation over 14 days (Fig. S16). When MMBs and hMSCs were co-loaded into the dHA hydrogel to form the dHAMBH hydrogel, both of them were uniformly distributed within the hydrogel. Under

standard culture conditions, the MMBs maintained structural stability with no observable diffusion (Fig. 3(i)). Quantitative analysis revealed that over a 14 days period neither US stimulation nor the presence of MMBs significantly affected the viability or proliferation of hMSCs (Fig. 3(j)). Therefore, these results suggest that the dHAMBH hydrogel exhibits excellent biocompatibility, making it a promising platform for tissue regeneration.

3.3 US-activated dHAMBH hydrogel enhances osteogenic differentiation of hMSCs *in vitro*

BMP-2 is a well-known osteogenic factor that promotes osteogenesis primarily through activation of the Smad signaling pathway, particularly through SMAD1 and SMAD4 [24]. In addition, IONPs can activate the mitogen-activated protein kinase (MAPK) signaling pathway [25, 26], thereby regulating downstream gene expression and further enhancing osteogenic differentiation. MMB-BMPs, composed of IONPs and BMP-2, were first evaluated for their pro-osteogenic effects *in vitro*. The hMSCs were treated with MMB-BMPs, individual components (IONPs or BMP-2), or osteogenic differentiation medium (low glucose-DMEM, 10% FBS, 100 U mL^{-1} penicillin-streptomycin, 10 nM dexamethasone, 10 mM sodium-β-glycerophosphate, and 0.05 mM ascorbic acid-2-phosphate) as a positive control (Fig. 4(a)). Alkaline phosphatase (ALP) activity, an early marker of osteo genic differentiation [23] was measured on 7, 10, and 14 days (Fig. 4(a)). Quantitative analysis of ALP activity revealed a time-dependent increase in all treated groups. Significantly higher ALP activity was observed in the MMB-BMPs treated group on day 14 compared to the other groups, which was attributed to the synergistic effects of IONPs and

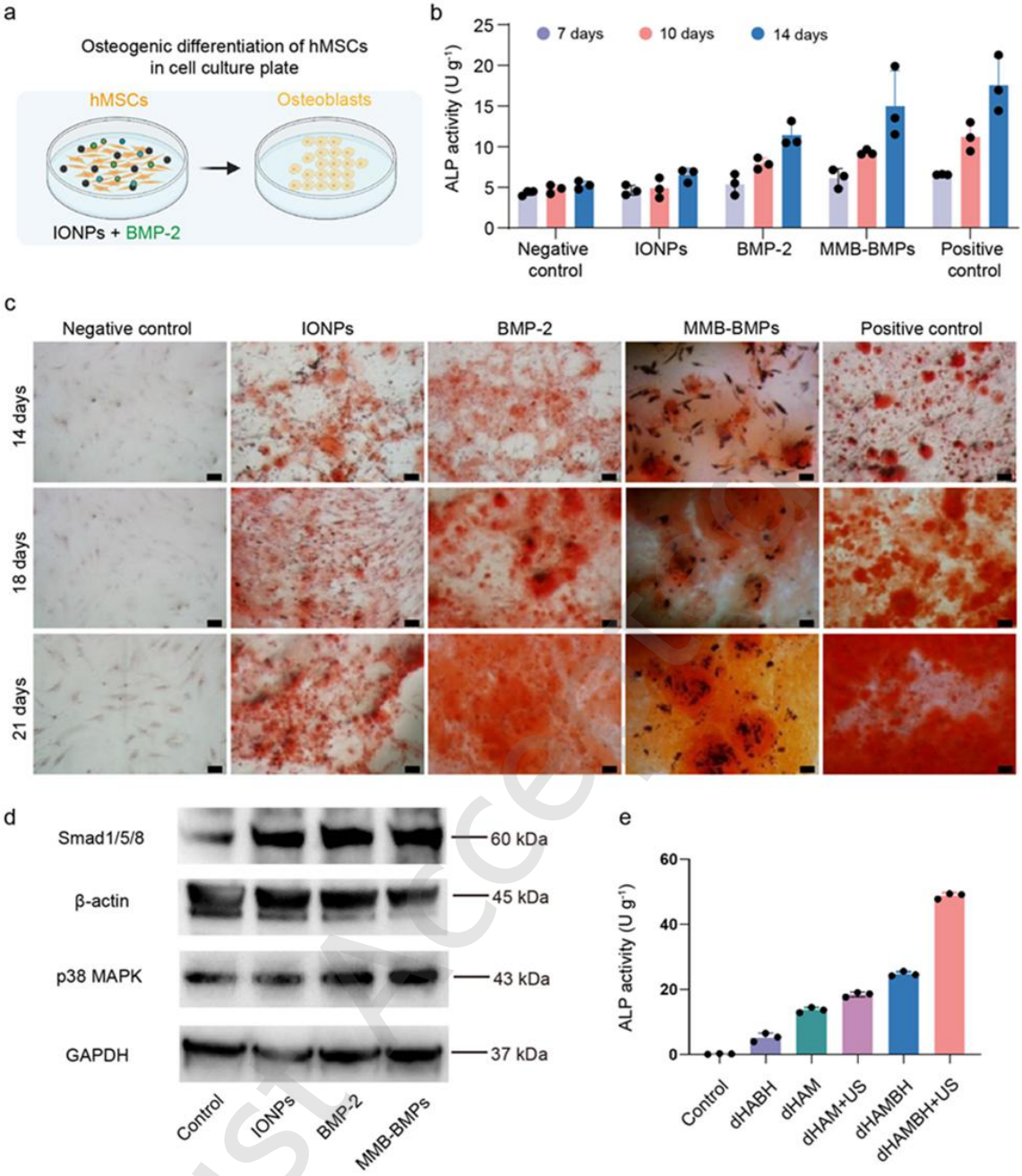

Figure 4 US-activated dHAMBH hydrogel enhances osteogenic differentiation of hMSCs in vitro. (a) Schematic illustration of the osteogenic differentiation of hMSCs in cell culture plates after different treatments. (b) Quantitative analysis of ALP activity in cell culture plates after different treatments on days 7, 10, and 14, n = 3. (c) Representative Alizarin Red staining (ARS) images of hMSCs after different treatments at various time points. Scale bars, 100 μm. (d) Representative Western blot images of Smad1/5/8 and p38 MAPK in hMSCs after different treatment. (e) Quantitative analysis of ALP activity in the transwell model after different treatments on day 14, n = 3. All data were expressed as the mean ± SD.

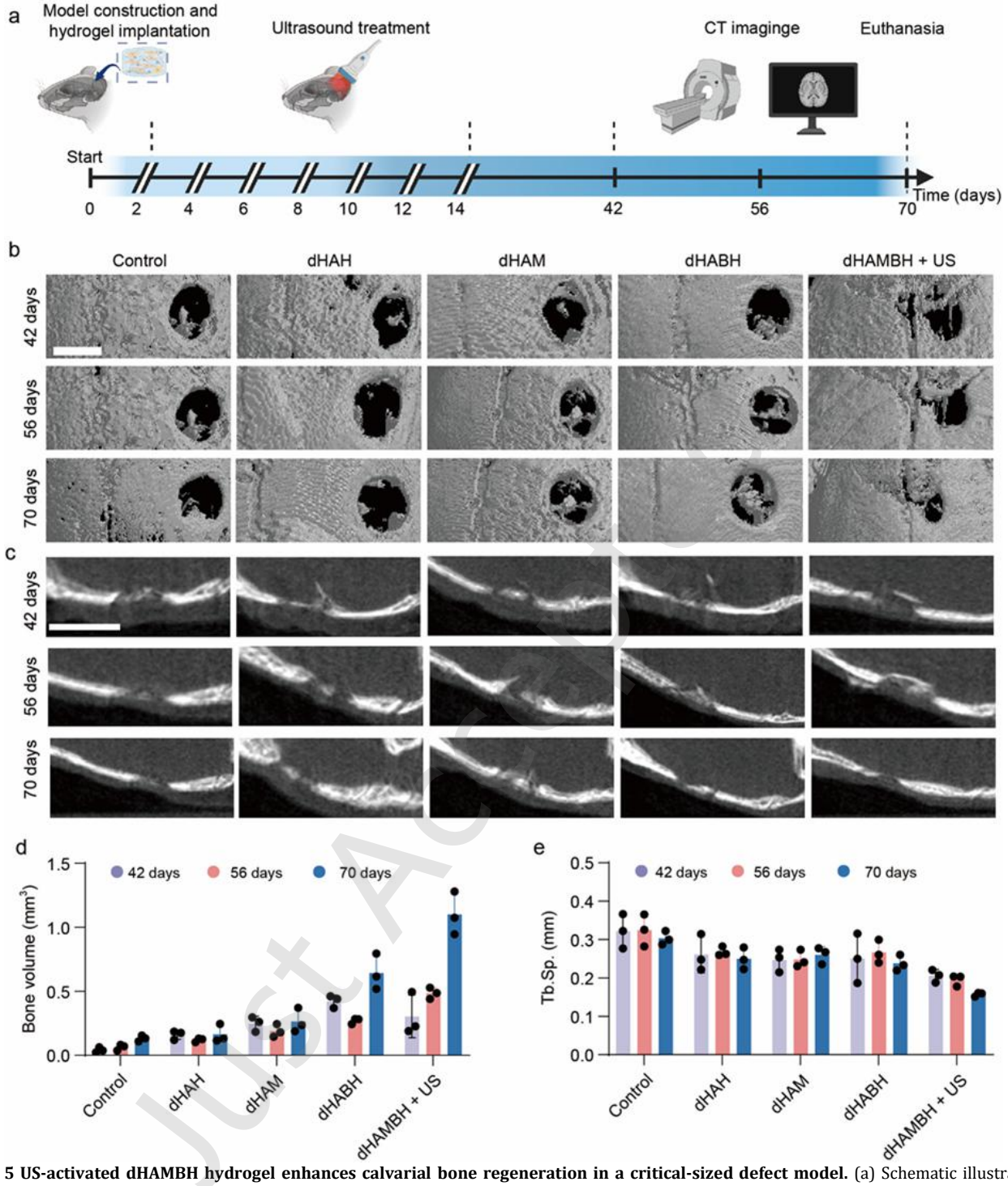

Figure 5 US-activated dHAMBH hydrogel enhances calvarial bone regeneration in a critical-sized defect model. (a) Schematic illustration o therapeutic schedule for calvarial bone regeneration in a critical-sized defect model. (b) Representative μCT images of the repair progress of calvaria bone structure following different treatments. Scale bar: 4 mm. (c) Representative coronal view images of bone defect repair after differen treatments. Scale bar: 4 mm. (d) Quantitative analysis of newly formed trabecular bone volume at different time points after treatment, n = 3. (e) Quantitative analysis of trabecular separation (Tb.Sp.) at different time points following different treatments, n = 3. All data were expressed as the mean ± SD.

BMP-2 (Fig. 4(b)). Next, Alizarin Red staining (ARS) was performed to assess mineralized nodule formation [27]. While both IONPs and BMP-2 individually enhanced mineral deposition, the MMB-BMPs treated group showed the strongest osteogenic response after 21 days, indicated by a more intense orange-red signal compared to the other groups (Fig. 4(c)). Western blot analysis further showed that treatment with MMB-BMPs or their individual components, IONPs and BMP-2, increased the levels of Smad1/5/8 and p38 MAPK in hMSCs, indicating activation of the osteogenesis-related SMAD and MAPK signaling pathways (Fig. 4d).To assess the osteogenic differentiation of hMSCs within the dHAMBH hydrogel after US stimulation, a transwell system was employed with cell culture medium in the lower chamber and the hydrogel samples placed in the upper chamber. US stimulation was applied every two days, and ALP activity of hMSCs was measured on day 14 (Fig. S17). As shown in Figure 4e, in the absence of US stimulation, the dHAMBH hydrogel (loaded with both BMP-2 and IONPs) exhibited enhanced ALP activity compared to the dHABH

hydrogel (loaded with BMP-2) and the dHAM hydrogel (loaded with IONPs). Notably, US stimulation of the dHAMBH hydrogel resulted in a 2-fold increase in ALP activity compared to the unstimulated condition (Fig. 4(e)). Furthermore, US had only a limited direct effect on osteogenic differentiation (Fig. 4(e)). Its major contribution was to promote the release and distribution of BMP-2 and IONPs within the hydrogel system, followed by their uptake by hMSCs, thereby enhancing osteogenic differentiation.

3.4 US-activated dHAMBH hydrogel enhances calvarial bone regeneration in a critical-sized defect model

Given that the dHAMBH hydrogel combined with US treatment effectively and sustainably promoted the osteogenic differentiation of hMSCs *in vitro*, we further evaluated the bone regeneration potential of the dHAMBH hydrogel combined with US in a mouse calvarial critical-sized defect model. A 4 mm critical-sized calvarial defect was created in mice [28] and subsequently filled with 100 μL of dHAMBH hydrogel containing hMSCs (2×10^6 cells mL^{-1}). The dHAMBH hydrogel, co-loaded with MMB-BMPs and hMSCs *in vitro*, was gelled in situ and filled the defect area. CLSM confirmed the uniform distribution of both components within the hydrogel matrix (Figure 3i). US treatment was applied every two days for t wo weeks post-implantation. Bone regeneration within the defect area was monitored using micro-computed tomography (μCT) [29] at 42, 56, and 70 days post-implantation (Fig. 5(a)). 3D reconstructions and sagittal views revealed that the combination of dHAMBH hydrogel and US treatment enhanced new bone formation, with regenerative effects becoming more pronounced over time. After 42 days, the defect area in the dHAMBH + US group (loaded with both BMP-2 and IONPs) was markedly smaller than in the dHABH (loaded with BMP-2), dHAM (loaded with IONPs), and dHAH (loaded with hMSCs) groups (Figs. 5(b) and 5(c)).

By day 70, coronal view images revealed nearly complete healing in the dHAMBH + US group. Quantitative analysis further confirmed that this group achieved a newly formed bone volume of 1.1 mm^3 at day 70 compared to the dHABH (0.64 mm^3), dHAM (0.27 mm^3), and dHAH (0.16 mm^3) groups, representing approximately 1.7-fold, 4.1-fold, and 6.7-fold increases, respectively (Fig. 5(d)). Moreover, trabecular separation (Tb.Sp.) analysis at day 70 revealed minimal change in the control group, slight reductions in the dHABH (0.24 mm), dHAM (0.26 mm), and dHAH (0.25 mm) treated groups, and the greatest decrease in the dHAMBH + US group (0.16 mm) (Fig. 5(e)). These results demonstrate that the dHAMBH hydrogel, when combined with US stimulation, markedly promotes calvarial bone regeneration. The osteogenic improvements observed in the dHAM group can be attributed to the stimulatory effects of IONPs on hMSCs differentiation. The dHABH group showed increased bone formation due to the direct action of BMP-2 in the absence of controlled release. In contrast, the dHAMBH + US group benefited from US-triggered, sustained release of BMP-2 and IONPs, resulting in progressively accelerated and enhanced bone regeneration.

3.5 Histology and immunohistochemical analysis of calvarial bone defects

At 70 days post-treatment, calvarial bone defects were harvested for histological analysis. Hematoxylin and eosin (H&E) staining and Masson's trichrome staining revealed that the dHAMBH hydrogel combined with US treatment led to a larger area of mineralized bone matrix within the defect site, indicating robust new bone formation. In contrast, partial fibrous tissue formation was observed in the dHABH, dHAM, and dHAH groups (Figs. 6a-6b and S18-S19). BMP-2 and IONPs promote osteoblastic differentiation by activating signaling pathways such as SMAD and MAPK, which upregulate the osteogenic-specific transcription factor runt-related transcription factor 2 (RUNX2) [30-32]. RUNX2 subsequently stimulates the expression of downstream osteogenic markers, including osteocalcin (OCN) and osteopontin (OPN) [22,33,34]. Immunohistochemical staining was performed to assess the expression of RUNX2, ALP, OCN, and OPN. The dHAMBH + US group exhibited a significantly larger positive staining area and greater abundance of all four markers compared to the other groups after 70 days (Figs. 6(c), S20-S23). Quantitative analysis of Masson's trichrome staining confirmed that, compared to the dHABH, dHAM, and dHAH groups, the dHAMBH + US group enhanced new bone formation, with bone areas increasing by 3.1-, 3.5-, and 6.7-fold, respectively (Fig. 6(d)). Analysis of RUNX2 positive cell ratios further supported these findings, showing 1.7-, 1.8-, and 3.1-fold increases compared to the respective controls (Fig. 6(e)). Similarly, the dHAMBH + US group showed the highest positive staining areas for ALP, OCN, and OPN (Fig. 6(f)). Staining intensity analysis based on integral optical density (IOD) further confirmed that the dHAMBH + US group has the strongest expression levels for these osteogenic proteins (Fig. 6(g)) [35]. Collectively, these results indicate that the dHAMBH hydrogel combined with US stimulation promotes osteogenic differentiation by gradually releasing IONPs and BMP-2, which synergistically upregulate RUNX2 and enhance the expression of ALP, OCN and OPN, thereby facilitating new bone formation within the calvarial defect and facilitates tissue regeneration.

In addition, hydrogel gradually degraded *in vivo* without causing obvious damage to the surrounding tissues (Fig. S24). Blood analysis revealed no significant differences in neutrophil, lymphocyte, monocyte, or white blood cell levels between the dHAMBH-treated group and the PBS control group, indicating minimal systemic immune response (Fig. S25). Moreover, H&E staining of major organs revealed no evidence of inflammation or toxicity (Fig. S26). These findings demonstrate the biocompatibility of the dHAMBH hydrogel *in vivo*.

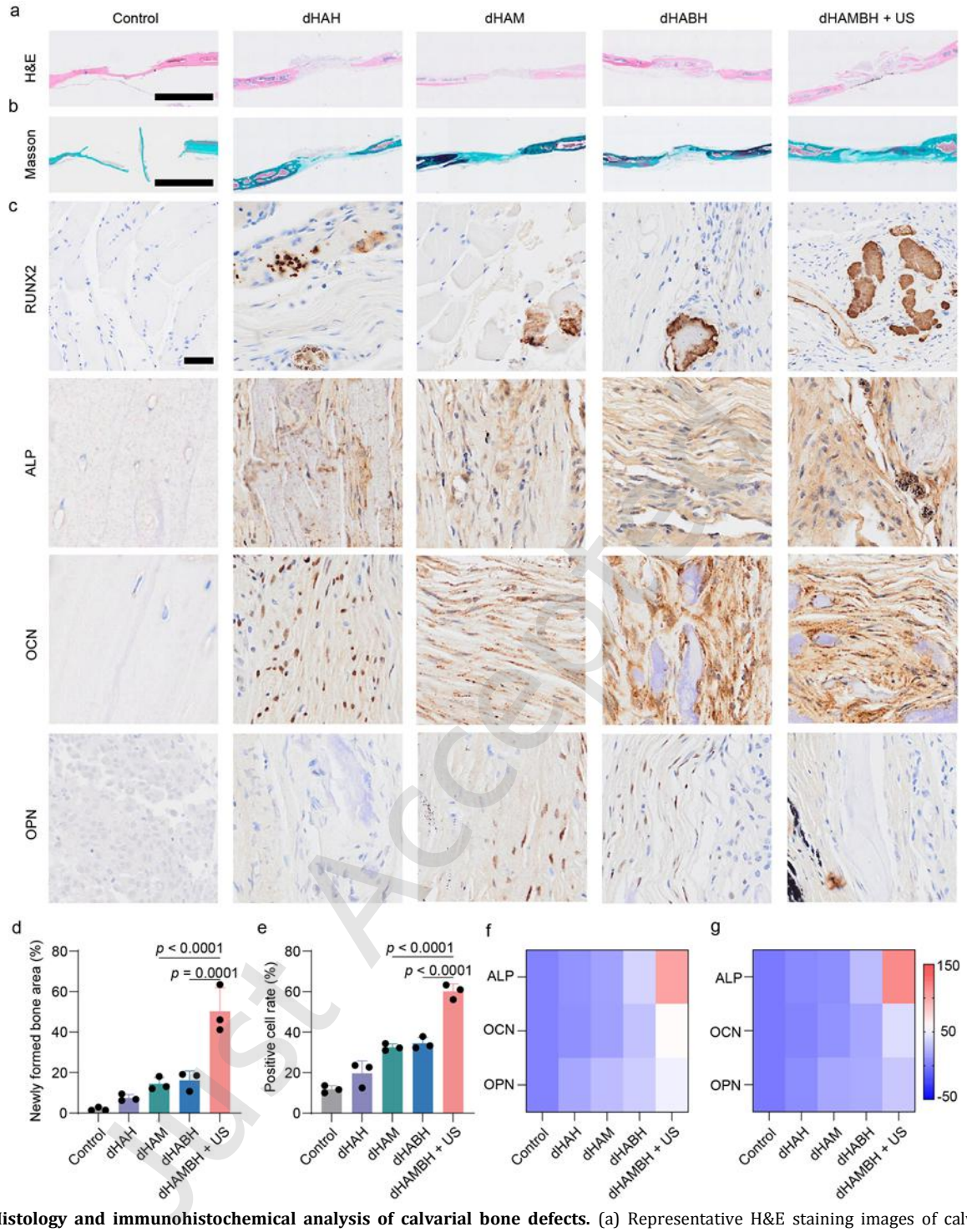

Figure 6 Histology and immunohistochemical analysis of calvarial bone defects. (a) Representative H&E staining images of calvarial defec following different treatments. Scale bar: 1 mm. (b) Representative Masson's staining images of calvarial defects after different treatments. Scale bar: 4 mm. (c) Representative immunohistochemical staining images for RUNX2, alkaline phosphatase (ALP), osteocalcin (OCN), and osteopontin (OPN) afte different treatments. Scale bar: 50 μm. (d) Quantitative analysis of newly formed bone area based on Masson's staining images, n = 3. (e) Quantitative analysis of RUNX2-positive cell ratios based on immunohistochemical staining images, n = 3. (f) Heatmaps displaying the positive staining areas of ALP OCN, and OPN based on immunohistochemical staining images. Results are normalized to the control group, n = 3. (g) Heatmaps displaying the integra optical density (IOD) values of ALP, OCN, and OPN based on immunohistochemical staining images. Results are normalized to the control group, n = 3 All data were expressed as the mean ± SD. Statistical significance was calculated by one-way ANOVA with the Tukey post hoc test.

4 Conclusions

In summary, we developed a US-responsive dynamic hydrogel platform for tissue regeneration. By integrating engineered MMB-BMPs into a self-reorganizing hydrogel scaffold, the platform enables US activated stable oscillation of MMB-BMPs at their resonant frequencies, achieving sustained, on-demand release of IONPs and BMP-2 while avoiding cavitation induced burst release. Meanwhile, the dynamic hydrogel exhibits excellent biocompatibility, supports hMSCs adhesion and viability, and preserves structural integrity after repeated US stimulation through network reorganization. Moreover, US-triggered release of IONPs and BMP-2 synergistically activated SMAD and MAPK signaling pathways, promotes osteogenic differentiation, and accelerates bone regeneration. Overall, this work provides a

promising strategy for precise, controllable, and efficient therapeutic delivery in regenerative medicine.

Data availability

All data needed to evaluate the conclusion in the paper are present in the paper and/or the Electronic Supplementary Material. Additional data related to this paper may be requested from the authors.

Acknowledgements

This work is granted by the Basic Research Program of Jiangsu (BK20253006， BK20243057) and the National Natural Science Foundation of China (22277058, 22575124 , 62235008, 62288102). C.X. appreciates the support by Innovation and Technology Fund from Innovation and Technology Commission of the Hong Kong Special Administrative Region China (GHP/066/22GD).

Declaration of competing interest

All the contributing authors report no conflict of interests in this work.

Author contribution statement

L. L. R.: Conceptualization, data curation, investigation, methodology, writing - original draft. J. Y. S.: Data curation, formal analysis, validation. Y. X. C.: Data curation, formal analysis. Z. X. W.: Data curation, formal analysis. L. M. T.: Investigation, validation. W. J. Y.: Conceptualization, methodology. L. X. W.: Investigation, validation. S. Y. W. (corresponding author): Conceptualization, formal analysis, visualization, writing - review & editing. C. J. X (corresponding author).: Conceptualization, funding acquisition, writing - review & editing. L. H. W. (corresponding author): Conceptualization, funding acquisition, project administration, supervision. Y. G. (corresponding author): Conceptualization, funding acquisition, methodology, project administration, supervision, writing - review & editing. All the authors have approved the final manuscript.

Informed consent

Not applicable.

Ethics statement

The animal experiments were carried out following the guidelines of the protocol approved by the Institute Animal Care and Use Committee of the Affiliated Drum Tower Hospital of Nanjing University Medical School (Protocol number: 2021AE02021).

Use of AI statement

None.

References

[1] Xue, X.; Hu, Y.; Deng, Y. H.; Su, J. C. Recent Advances in Design of Functional Biocompatible Hydrogels for Bone Tissue Engineering. *Adv. Funct. Mater.* **2021**, 31, 2009432.

[2] Zhou, L. M.; Liu, H. L.; Zhang, B. R.; Wei, C. X.; Zhou, S. H.; Huang, X. Y.; Zhong, X. X.; Zhang, L.; Bi, W.; Liu, J. H.; Liang, Y. Z.; Jin, L.; Guo, R. A Novel 3D-printed Bi-Layer Cranial-Brain Patch Promotes Brain Injury Repair and Bone Tissue Regeneration. *Adv. Funct. Mater.* **2024**, 34, 2314330.

[3] Mochizuki, M.; Guc, E.; Park, A. J.; Julier, Z.; Briquez, P. S.; Kuhn, G. A.; Muller, R.; Swartz, M. A.; Hubbell, J. A.; Martino, M. M. Growth Factors with Enhanced Syndecan Binding Generate Tonic Signalling and Promote Tissue Healing. *Nat. Biomed. Eng.* **2020**, 4, 463-475.

[4] Chen, T.; Jiang, Y.; Huang, J. P.; Wang, J.; Wang, Z. K.; Ding, P. H. Essential Elements for Spatiotemporal Delivery of Growth Factors within Bio-scaffolds: A Comprehensive Strategy for Enhanced Tissue Regeneration. *J. Control. Release* **2024**, 368, 97-114.

[5] Freeman, F. E.; Pitacco, P.; van Dommelen, L. H. A.; Nulty, J.; Browe, D. C.; Shin, J.Y.; Alsberg, E.; Kelly, D. J. 3D Bioprinting Spatiotemporally Defined Patterns of Growth Factors to Tightly Control Tissue Regeneration. *Sci. Adv.* **2020**, 6, eabb5093.

[6] Ho, S. S.; Vollmer, N. L.; Refaat, M. I.; Jeon, O.; Alsberg, E.; Lee, M. A.; Leach, J. K. Bone Morphogenetic Protein-2 Promotes Human Mesenchymal Stem Cell Survival and Resultant Bone Formation when Entrapped in Photocrosslinked Alginate Hydrogels. *Adv. Healthc. Mater.* **2016**, 5, 2501-2509.

[7] Bez, M.; Sheyn, D.; Tawackoli, W.; Avalos, P.; Shapiro, G.; Giaconi, J. C.; Da, X. Y.; David, S. B.; Gavrity, J.; Awad, H. A.; Bae, H. W.; Ley, E. J.; Kremen, T. J.; Gazit, Z.; Ferrara, K. W.; Pelled, G.; Gazit, D. In Situ Bone Tissue Engineering via Ultrasound-mediated Gene Delivery to Endogenous Progenitor Cells in Mini-Pigs. *Sci. Transl. Med.* **2017**, 9, eaal3128.

[8] Chen, Y. S.; Zhao, Y.; Beinat, C.; Zlitni, A.; Hsu, E. C.; Chen, D. H.; Achterberg, F.; Wang, H. W.; Stoyanova, T.; Dionne, J.; Gambhir, S. S. Ultra-high-frequency radio-frequency acoustic molecular imaging with saline nanodroplets in living subjects. *Nat. Nanotechnol.* **2021**, 16, 717-724.

[9] Song, R. J.; Zhang, C. B.; Teng, F. M.; Tu, J.; Guo, X. S.; fan, Z.; Zheng, Y. F.; Zhang, D. Cavitation-facilitated transmembrane permeability enhancement induced by acoustically vaporized nanodroplets. *Ultrason. Sonochem.* **2021**, 79, 105790.

[10] Wang, S. Y.; Guo, X. X.; Xiu, W. J.; Liu, Y.; Ren, L. L.; Xiao, H. X.; Yang, F.; Gao, Y.; Xu, C. J.; Wang, L. H. Accelerating Thrombolysis using a Precision and Clot-Penetrating Drug Delivery Strategy by Nanoparticle-shelled Microbubbles. *Sci. Adv.* **2020**, 6, eaaz8204.

[11] Gao, Y.; Chan, C. U.; Gu, Q. S.; Lin, X. D.; Zhang, W. C.; Yeo, D. C. L.; Alsema, A. M.; Arora, M.; Chong, M. S. K.; Shi, P.; Ohl, C. D.; Xu, C. J. Controlled Nanoparticle Release from Stable Magnetic Microbubble Oscillations. *NPG Asia Mater.* **2016**, 8, e260-e260.

[12] Yang, L.; He, X. L.; Cai, L. J.; Zhao, Y. J. Emerging Hydrogel-Based Systems for Stem Cell Delivery and Bone Repair. *Adv. Funct. Mater.* **2026**, 0, e00014

[13] Caprio, N. D.; Davidson, M. D.; Daly, A. C.; Burdick, J. A. Injectable MSC Spheroid and Microgel Granular Composites for Engineering *Tissue. Adv. Mater.* **2024**, 36, e2312226.

[14] Loveland, S. J.; Tong, X. M.; Ayushman, M.; Lee, H. P.; Johannsen, J. M.; Weber, C. M.; Song, J.; Tai, M.; Mikos, G.; Chaib, Y.; Chaudhuri, O.; Yang, F. Adaptable Sliding Hydrogels Enable Pericellular Pocket Formation while Enhancing MSC Chondrogenesis and Survival in 3D. *Bioact. Mater.* **2026**, 62, 480-494.

[15] Feng, Q.; Xu, J. K.; Zhang, K. Y.; Yao, H.; Zheng, N. Y.; Zheng, L. Z.; Wang, J. L.; Wei, K. C.; Xiao, X. F.; Qin, L.; Bian, L. M. Dynamic and Cell-Infiltratable Hydrogels as Injectable Carrier of Therapeutic Cells and Drugs for Treating Challenging Bone Defects. *ACS Cent. Sci.* **2019**, 5, 440-450.

[16] Kang, H. M.; Zhang, K. Y.; Jung, H. J.; Yang, B. G.; Chen, X. Y.; Pan, Q.; Li, R.; Xu, X. Y.; Li, G.; Dravid, V. P.; Bian, L. M. An in Situ Reversible Heterodimeric Nanoswitch Controlled by Metal-Ion–Ligand Coordination Regulates the Mechanosensing and Differentiation of Stem Cells. *Adv. Mater.* **2018**, 30, e1803591.

[17] Wojtecki, R. J.; Meador, M. A.; Rowan, S. J. Using the Dynamic Bond to Access Macroscopically Responsive Structurally Dynamic Polymers. *Nat. Mater.* **2011**, 10, 14-27.

[18] Zhang, K. Y.; Feng, Q.; Fang, Z. W.; Gu, L.; Bian, L. M. Structurally Dynamic Hydrogels for Biomedical Applications: Pursuing a Fine Balance between Macroscopic Stability and Microscopic Dynamics. *Chem. Rev.* **2021**, 121, 11149-11193.

[19] Qin, H. L.; Zhang, T.; Li, N.; Cong, H. P.; Yu, S. H. Anisotropic and Self-Healing Hydrogels with Multi Responsive Actuating Capability. *Nat. Commun.* **2019**, 10, 2202.

[20] Chen, C. W.; Wang, Y.; Zhang, H.; Zhang, H.; Dong, W. L.; Sun, W. J.; Zhao, Y. J. Responsive and Self-Healing Structural Color Supramolecular Hydrogel Patch for Diabetic Wound Treatment. *Bioact. Mater.* **2022**, 15, 194-202.

[21] Zhang, L. Y.; Ma, M. J.; Li, J. F.; Qiao, K.; Xie, Y. J.; Zheng, Y. D. Stimuli-Responsive Microcarriers and their Application in Tissue Repair: A Review of Magnetic and Electroactive Microcarrier. *Bioact. Mater.* **2024**, 39, 147-162.

[22] Nimmo, C. M.; Owen, S. C.; Shoichet, M. S. Diels-Alder Click Cross-Linked Hyaluronic Acid Hydrogels for Tissue Engineering. *Biomacromolecules* **2011**, 12, 824-830.

[23] Li, Y.; Chen, S. K.; Li, L.; Qin, L.; Wang, X. L.; Lai, Y. X. Bone Defect Animal Models for Testing Efficacy of Bone Substitute Biomaterials. *J. Orthop. Translat.* **2015**, 3, 95-104.

[24] Wang, Q. W.; Chen, B.; Cao, M.; Sun, J. F.; Wu, H.; Zhao, P.; Xing, J.; Yang, Y.; Zhang, X. Q.; Ji, M.; Gu, N. Response of MAPK Pathway to Iron Oxide Nanoparticles in Vitro Treatment Promotes Osteogenic Differentiation of hBMSCs. *Biomaterials* **2016**, 86, 11-20.

[25] Wu, Y. T.; Zhou, C. C.; Xie, J.; Mo, A. C.; Lee, D.; Zhang, C. L.; Salas-Hernandez, J. L.; Qian, Z. Y.; Li, P.; Liao, J. F. Functional Iron Oxide Nanoparticles Cross-Linked Hydrogel for Craniofacial Bone Regeneration. *Biomaterials* **2026**, 327, 123782.

[26] Wang, T. Q.; Zhao, H. Q.; Jing, S. Z.; Fan, Y.; Sheng, G. H.; Ding, Q.; Liu, C. X.; Wu, H.; Liu, Y. Magnetofection of miR-21 Promoted by Electromagnetic Field and Iron Oxide Nanoparticles via the p38 MAPK Pathway Contributes to Osteogenesis and Angiogenesis for Intervertebral Fusion. *J. Nanobiotechnology* **2023**, 21, 27.

[27] Bouxsein, M. L.; Boyd, S. K.; Christiansen, B. A.; Guldberg, R. E.; Jepsen, K. J.; Muller, R. Guidelines for Assessment of Bone Microstructure in Rodents Using Micro-Computed Tomography. J. *Bone Miner. Res.* **2010**, 25, 1468-86.

[28] Klintstrom, E.; Smedby, O.; Klintstrom, B.; Brismar, T. B.; Moreno, R. Trabecular Bone Histomorphometric Measurements and Contrast-to-Noise Ratio in CBCT. *Dentomaxillofac. Radiol.* **2014**, 43, 20140196.

[29] Kang, H. R.; da Costa Fernandes, C. J.; da Silva, R. A.; Constantino, V. R. L.; Koh, I. H. J.; Zambuzzi, W. F. Mg-Al and Zn-Al Layered Double Hydroxides Promote Dynamic Expression of Marker Genes in Osteogenic Differentiation by Modulating Mitogen-Activated Protein Kinases. *Adv. Healthc. Mater.* **2018**, 7, 1700693.

[30] Rahman, M. S.; Akhtar, N.; Jamil, H. M.; Banik, R. S.; Asaduzzaman, S. M. TGF-b/BMP Signaling and Other Molecular Events: Regulation of Osteoblastogenesis and Bone Formation. *Bone Res.* **2015**, 3, 15005.

[31] Zeng, W. F.; Yan, Y.; Zhang, F. Y.; Zhang, C. L.; Liang, W. Chrysin Promotes Osteogenic Differentiation via ERK/MAPK Activation. *Protein Cell* **2013**, 4, 539-547.

[32] Zhao, M.; Chen, X. L.; Wang, W. Y.; Li, M. Y.; Zhang, H.; Zou, X. Q.; Wang, J. M.; Cong, Q.; Ma, X. Y.; Hou, Z. Y.; Lin, H. D.; Jia, H. Sea Buckthorn-Derived Extracellular Vesicles Foster Bone Regeneration Through aau-miR168-Mediated Pathways. *Stem Cell Res. Ther.* **2025**, 16, 281.

[33] Dong, Q.; Fu, H. Y.; Li, W. X.; Ji, X. Y.; Yin, Y. C.; Zhang, Y. R.; Zhu, Y. B.; Li, G. Q.; Jia, H. Y.; Zhang, H.; Wang, H. F.; Hu, J. L.; Wang, G. G.; Wu, Z. H.; Zhang, Y. Z.; Xu, S. J.; Hou, Z. Y. Nuclear Farnesoid X Receptor Protects Against Bone Loss by Driving Osteoblast Differentiation Through Stabilizing RUNX2. *Bone Res.* **2025**, 13, 20.

[34] Liu, W. Q.; Zhou, L. Y.; Zhou, C. C.; Zhang, S. W.; Jing, J. J.; Xie, L.; Sun, N. Y.; Duan, X. B.; Jing, W.; Liang, X.; Zhao, H.; Ye, L.; Chen, Q. M.; Yuan, Q. GDF11 Decreases Bone Mass by Stimulating Osteoclastogenesis and Inhibiting Osteoblast Differentiation. *Nat. Commun.* **2016**, 7, 12794.

[35] Li, L. M.; Li, Q.; Gui, L.; Deng, Y.; Wang, L.; Jiao, J. L.; Hu, Y. R.; Lan, X. Q.; Hou, J. H.; Li, Y.; Lu, D. Sequential Gastrodin Release PU/n-HA Composite Scaffolds Reprogram Macrophages for Improved Osteogenesis and Angiogenesis. *Bioact. Mater.* **2023**, 19, 24-37.

Electronic Supplementary Material

Dynamic hydrogels with repeatable ultrasound-activated microbubble oscillation enable stepwise spatiotemporal growth factor release for tissue regeneration

Lili Ren[1], Jingyi Su[1], Yuxuan Chen[1], Zhixuan Wang[1], Li Min Tay[2], Wenjing Yang[1], Lixing Weng[1], Siyu Wang [1] ✉, Chenjie Xu [3] ✉, Lianhui Wang [1] ✉, and Yu Gao [1] ✉

[1]*State Key Laboratory of Flexible Electronics (LoFE) & Jiangsu Key Laboratory of Smart Biomaterials and Theranostic Technology, Institute of Advanced Materials (IAM), Nanjing University of Posts & Telecommunications, Nanjing 210023, China*
[2]*School of Chemical and Biomedical Engineering, Nanyang Technological University, Singapore 639798, Singapore*
[3]*Department of Biomedical Engineering, College of Biomedicine, City University of Hong Kong, Kowloon Tong, Hong Kong 999077, China*

Supporting information to https://doi.org/10.26599/NR.2026.94909107

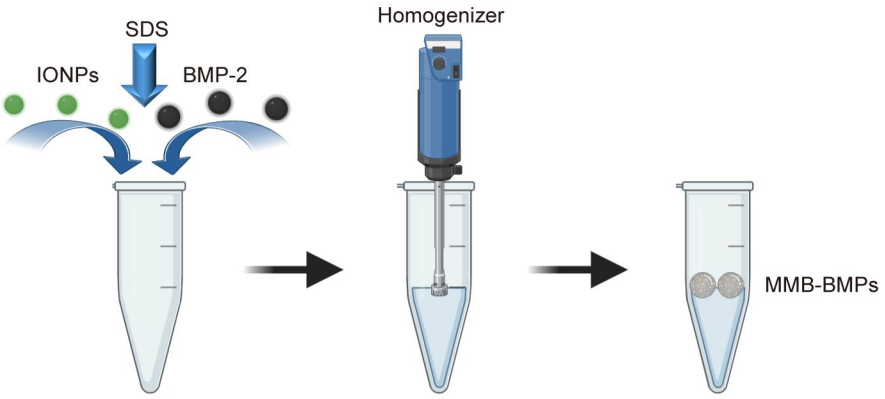

Figure S1 Schematic illustration of the synthesis process for MMB-BMPs.

Address correspondence to First A. Firstauthor, email1; Third C. Thirdauthor, email2

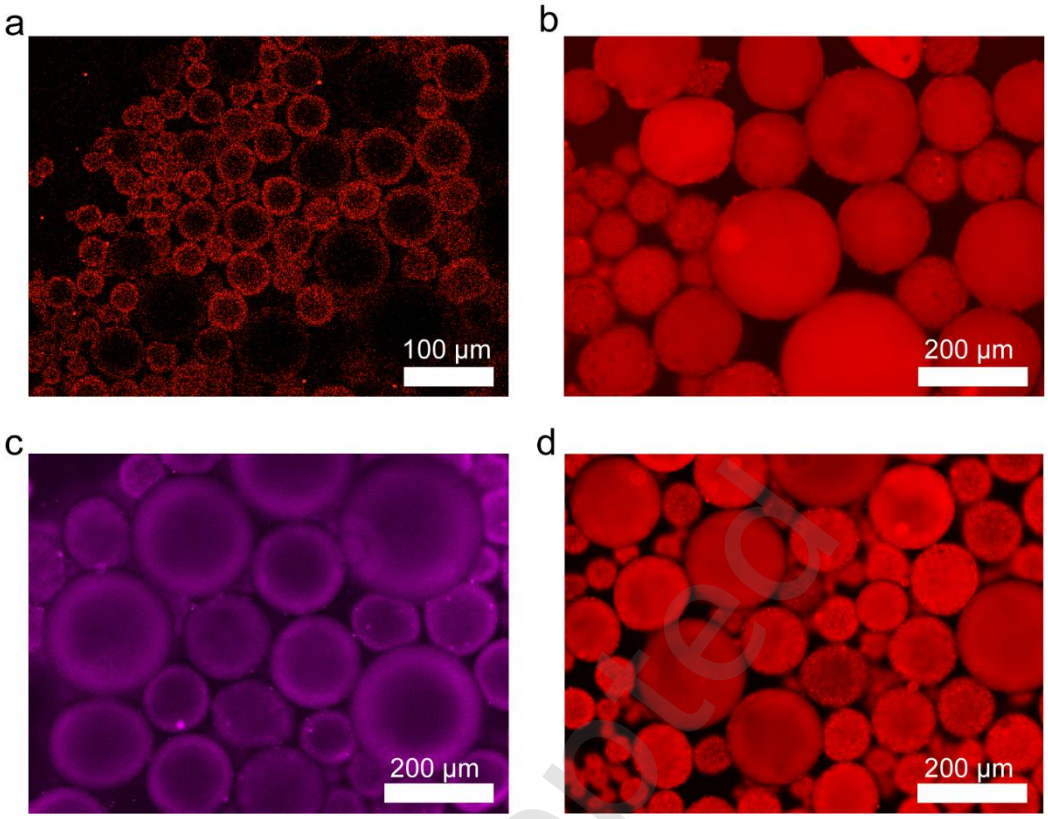

Figure S2 Representative CLSM images of MMBs loaded with different cargos: (a) doxorubicin, (b) glycosylphosphatidylinositol (GPI)-anchored proteins labelled with tdTomato, (c) Cy5-labeled silica nanoparticles (SiO2-Cy5), and (d) rhodamine-labeled polystyrene microspheres.

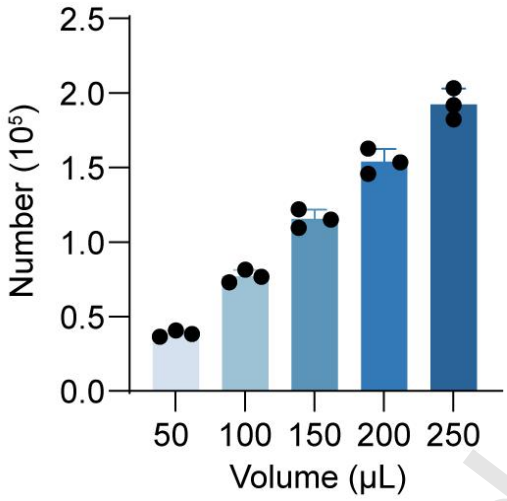

Figure S3 Quantification of the number of MMB-BMPs in different solution volumes, n = 3. All data were expressed as the mean ± SD.

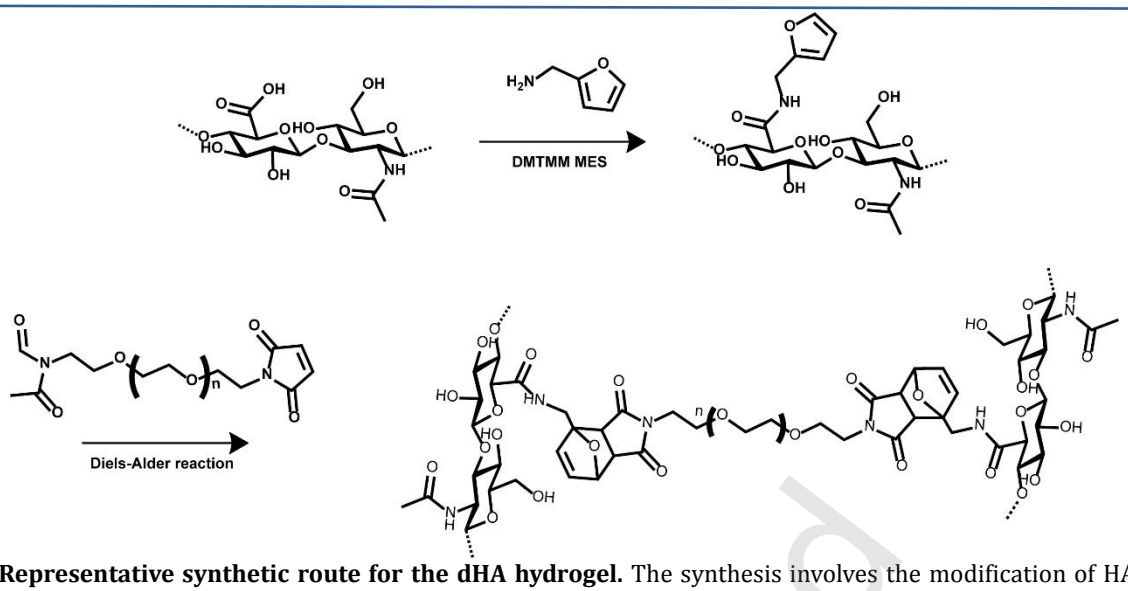

Figure S4 Representative synthetic route for the dHA hydrogel. The synthesis involves the modification of HA with furan groups using 4-(4,6-dimethoxy-1,3,5-triazin-2-yl)-4-methylmorpholinium chloride (DMTMM) in MES buffer to obtain HA-furan, followed crosslinking with a bifunctional MAL-PEG-MAL by D-A reaction to form the dHA hydrogel.

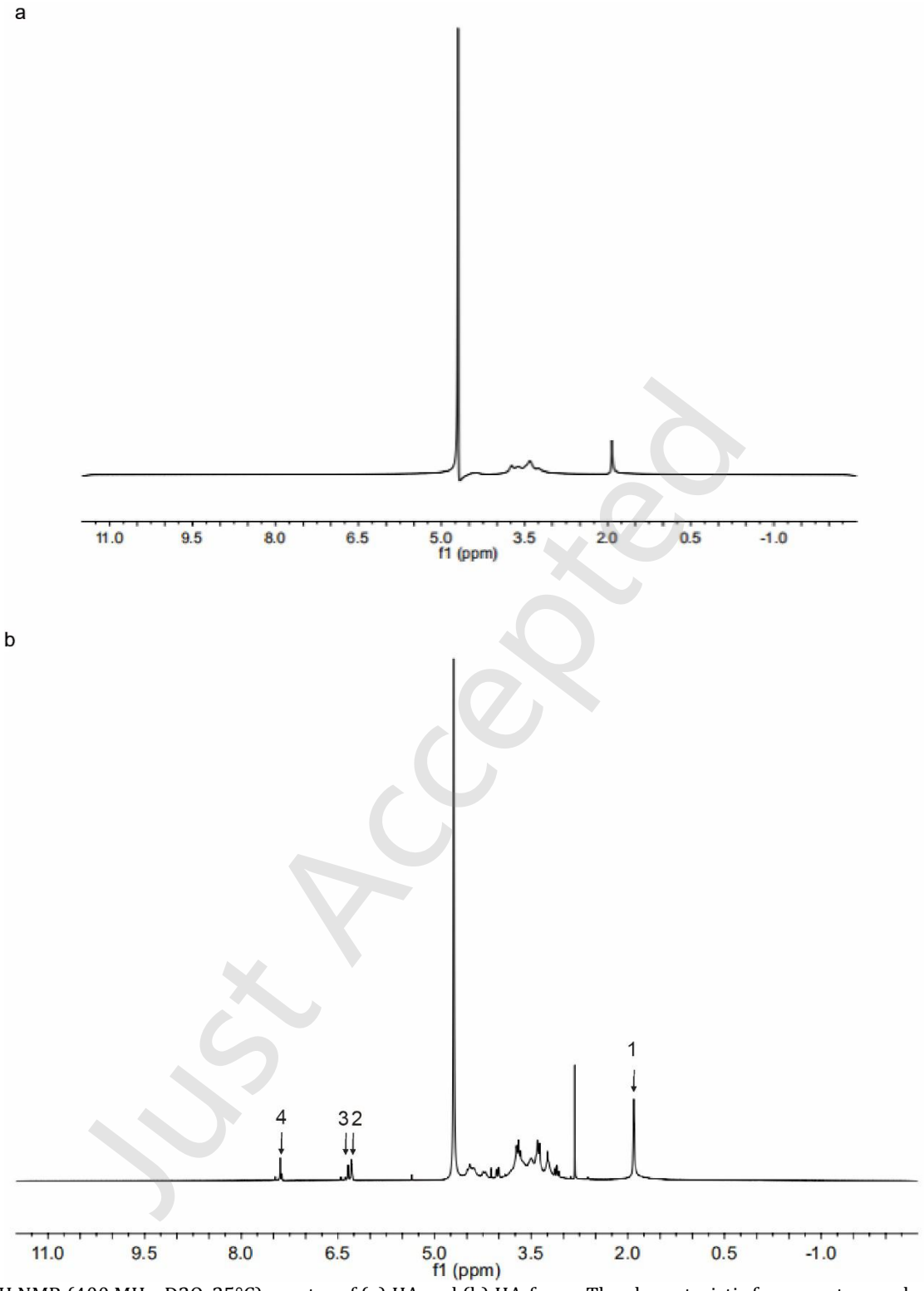

Figure S5 ^{1}H NMR (400 MHz, D2O, 25°C) spectra of (a) HA and (b) HA-furan. The characteristic furan proton peaks at 6.26, 6.46, and 7.65 ppm (labeled 2, 3, and 4) are shown relative to the peak at 1.9 ppm from the N-acetyl group of glucosamine in HA (labeled 1).

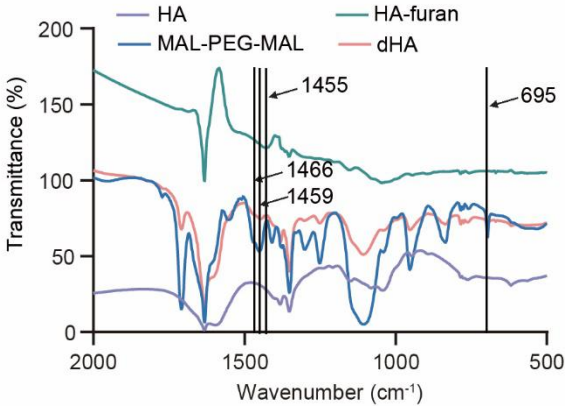

Figure S6 FTIR spectra of HA, HA-furan showing the C=C absorbance from furan at 1455 cm^{-1}, MAL-PEG-MAL showing the C=C absorbance from maleimide at 1466 cm^{-1} and =C-H bending at 695 cm^{-1}, and the resulting dHA hydrogel showing a decrease in both the 695, 1455, and 1466 cm^{-1} peaks and the appearance of a new peak at 1459 cm^{-1} corresponding to the C=C bond in the Diels-Alder adduct.

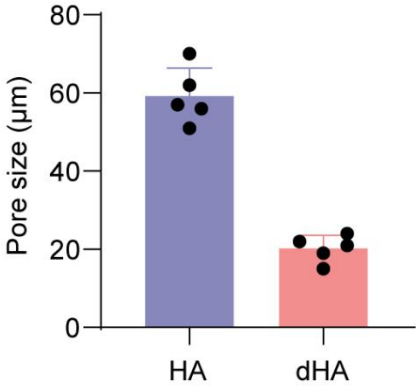

Figure S7 Quantitative analysis of pore sizes in HA and dHA hydrogels. The dHA hydrogel was formed by crosslinking HA-furan with MAL-PEG-MAL, n = 5. All data were expressed as the mean ± SD.

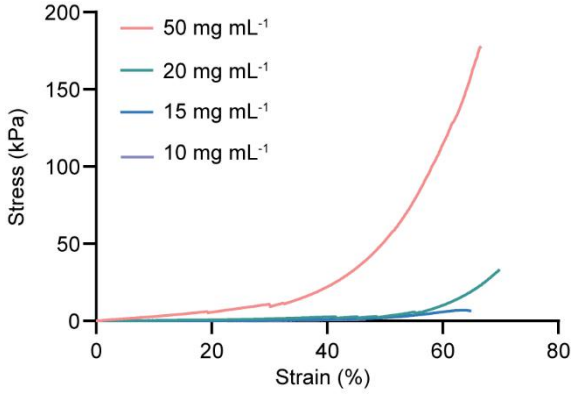

Figure S8 Compression stress-strain curves of dHA hydrogels with different concentrations of HA-furan.

Figure S9 Representative images demonstrating the injectability and shape adaptability of dHA hydrogels. Left: Rhodamine-labeled dHA hydrogel extruded through a 30G needle to assess injectability. Right: dHA hydrogels formed into various shapes, labeled with rhodamine and trypan blue.

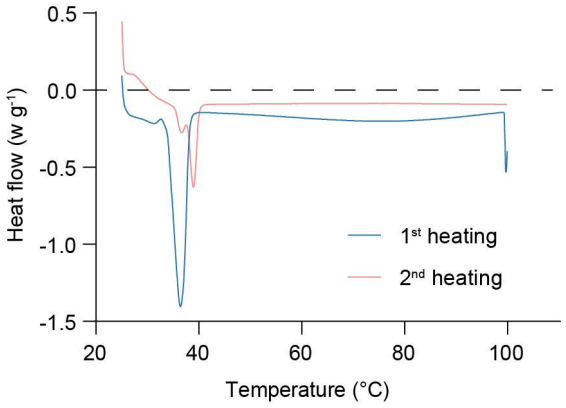

Figure S10 DSC curve of dHA hydrogel obtained using a heating-cooling-reheating cycle.

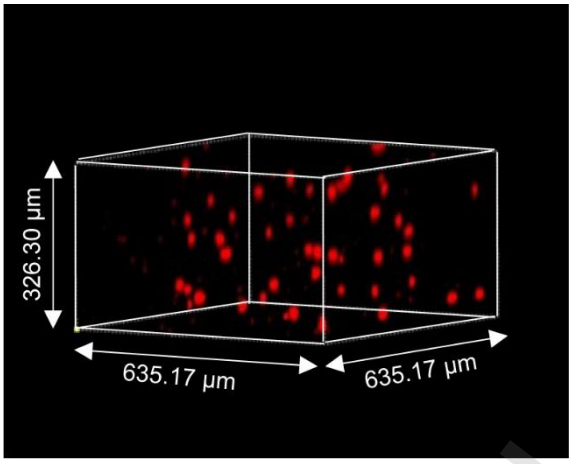

Figure S11 Representative 3D CLSM image of Cy5.5 labeled MMBs embedded in the dHA hydrogel.

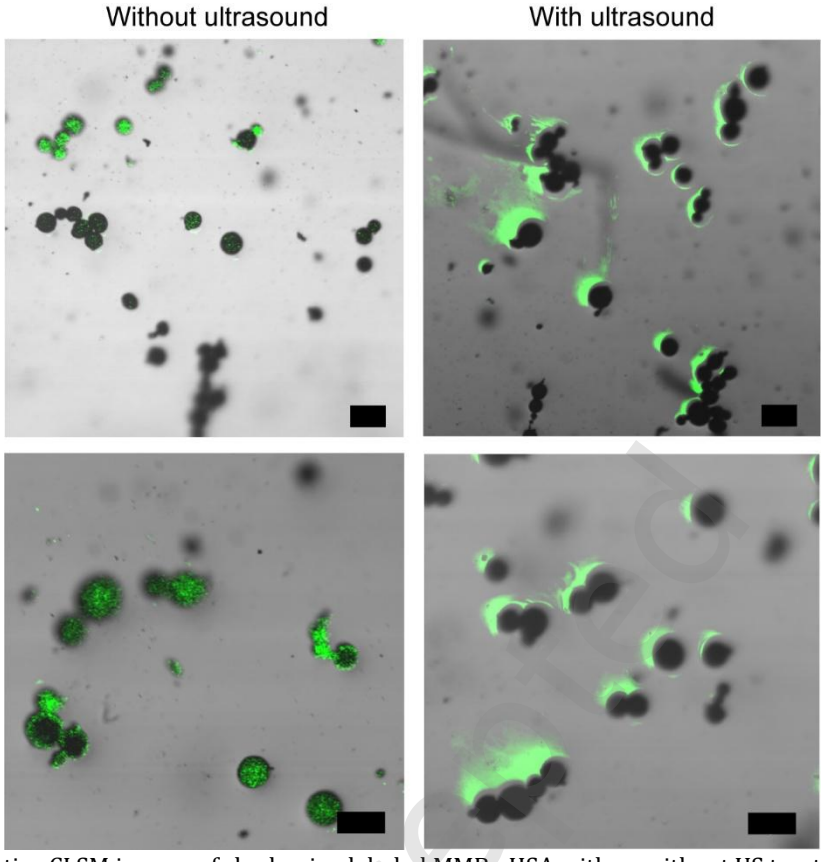

Figure S12 Representative CLSM images of rhodamine labeled MMBs-HSA with or without US treatment. Scale bars: 50 μm.

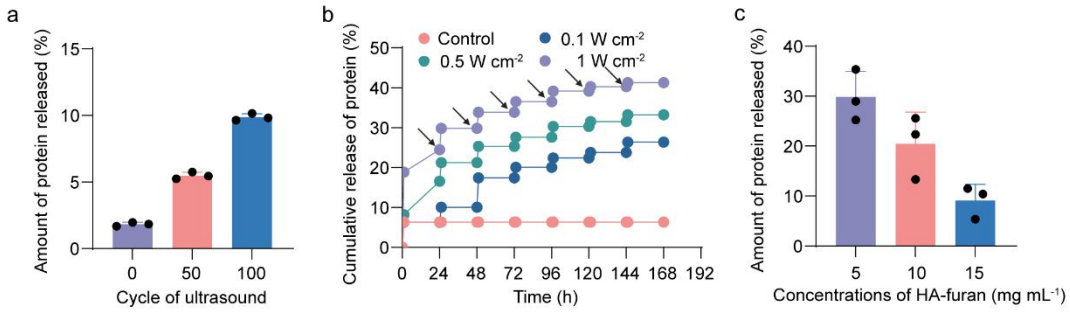

Figure S13 US controlled protein release from dHA hydrogels. (a) Amount of protein released from dHA hydrogels after different numbers of US cycles stimulation, n = 3. (b) Cumulative protein release profiles from the dHA hydrogel under different US intensities, with 50 cycles per treatment; black arrows indicate US stimulation. (c) Amount of protein released from dHA hydrogels with different concentrations of HA-furan, n = 3. All data were expressed as the mean ± SD.

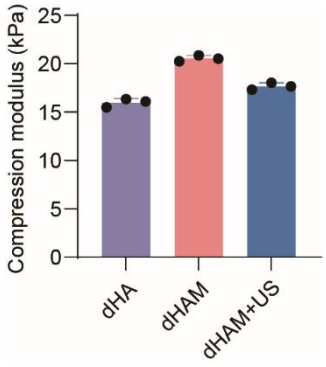

Figure S14 Quantification of the compressive modulus of the hydrogels before and after US-triggered cargo release, n = 3. All data were expressed as the mean ± SD

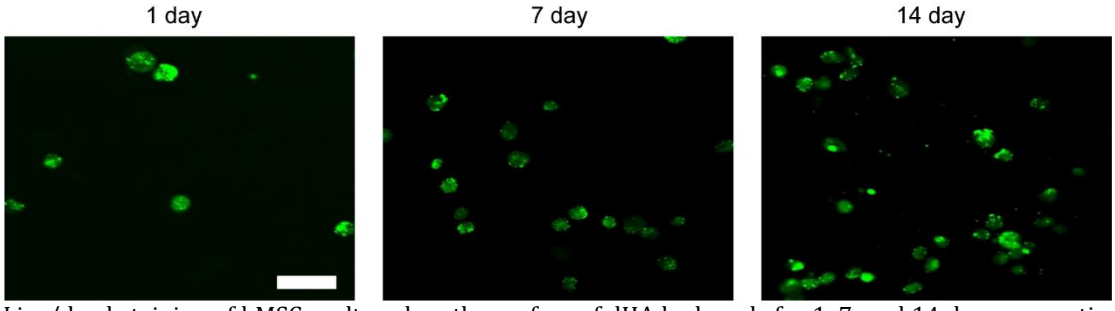

Figure S15 Live/dead staining of hMSCs cultured on the surface of dHA hydrogels for 1, 7, and 14 days, respectively. Scale bar: 200 μm.

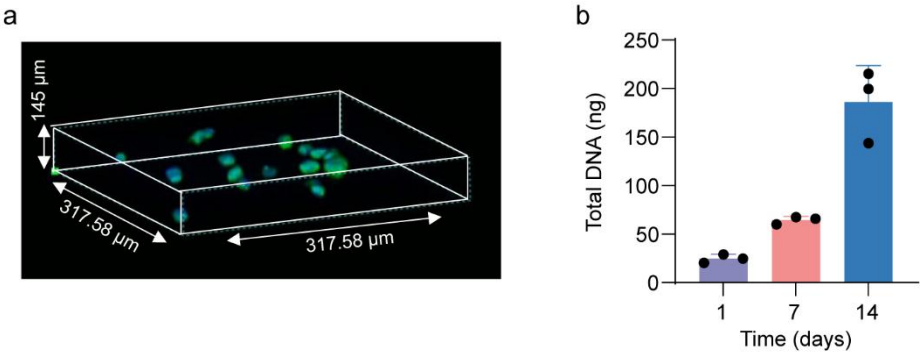

Figure S16 Biocompatibility of dHAH hydrogel. (a) Representative 3D CLSM image of the hMSCs loaded within the dHAH hydrogel. Blue: cell nucleus, green: cytoplasm. (b) Quantification of total DNA content to assess hMSC proliferation within the dHAH hydrogel after 14 days, n =3. All data were expressed as the mean ± SD.

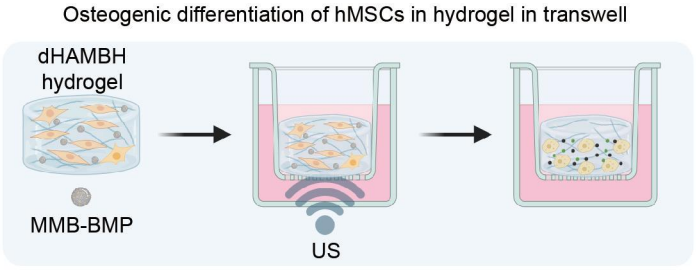

Figure S17 Schematic illustration of the osteogenic differentiation of hMSCs in a transwell model after different treatments.

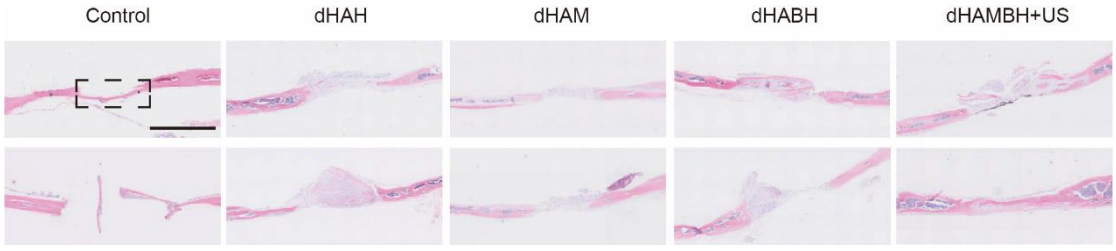

Figure S18 Representative H&E staining images of calvarial defects after different treatments. Scale bar: 4 mm. Black dashed box indicates the defect area.

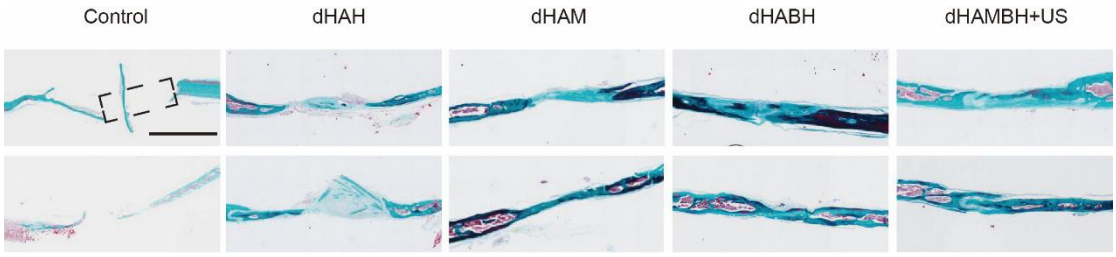

Figure S19 Representative Masson's staining images of calvarial defects after different treatments. Scale bar: 4 mm. Black dashed box indicates the defect area.

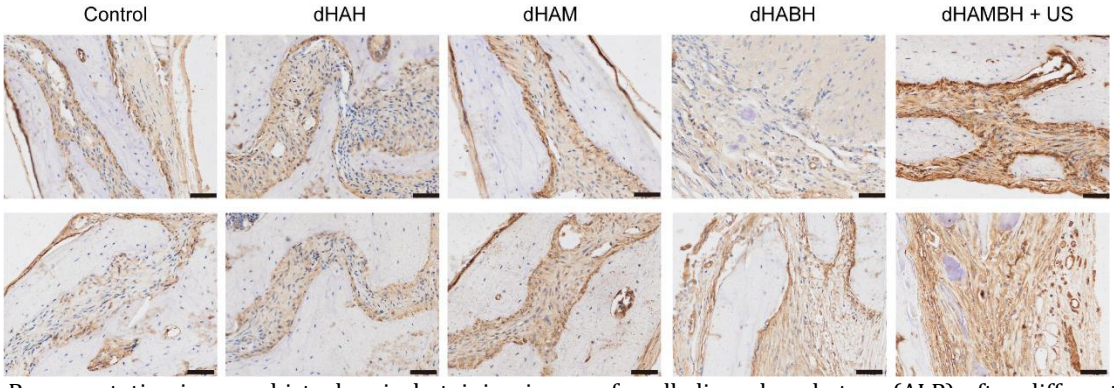

Figure S20 Representative immunohistochemical staining images for alkaline phosphatase (ALP) after different treatments. Scale bars: 50 μm.

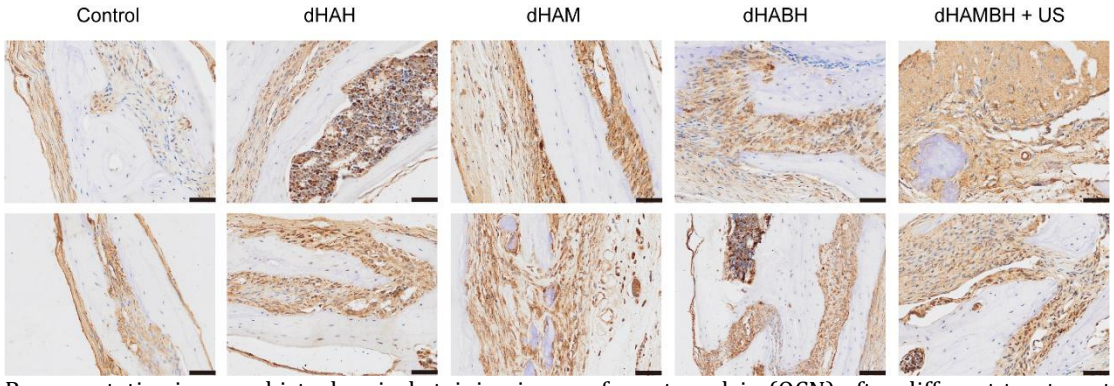

Figure S21 Representative immunohistochemical staining images for osteocalcin (OCN) after different treatments. Scale bars: 50 μm.

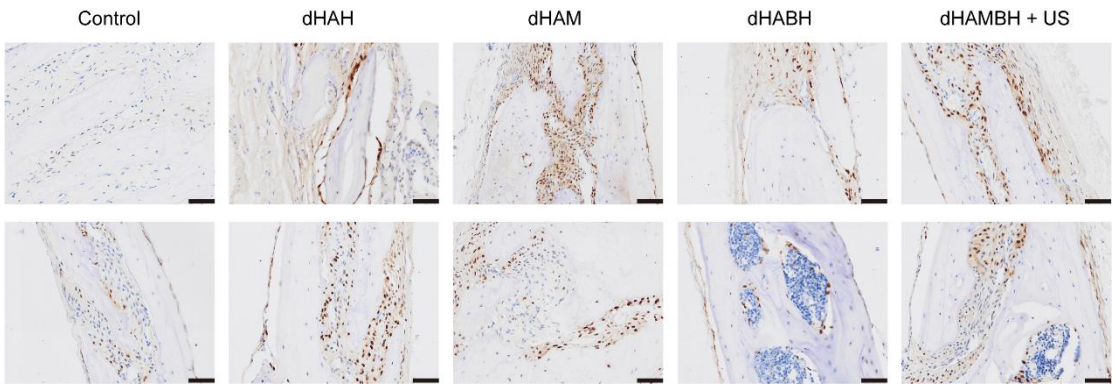

Figure S22 Representative immunohistochemical staining images for RUNX2 after different treatments. Scale bars: 50 μm.

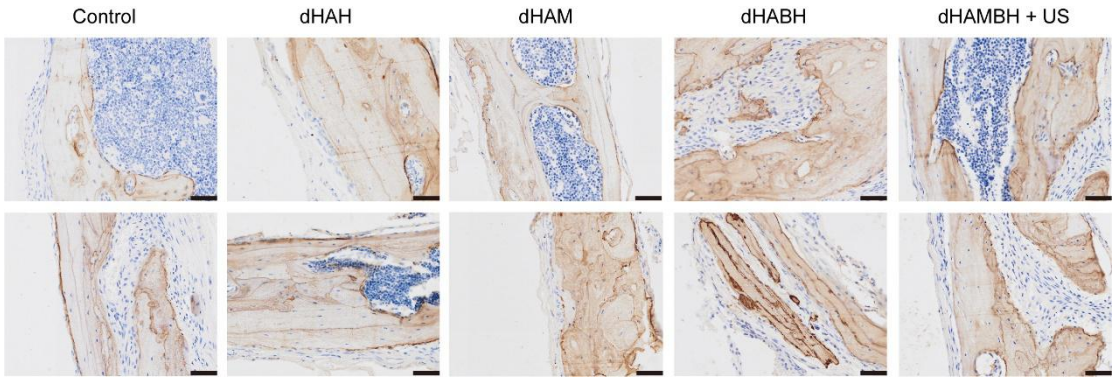

Figure S23 Representative immunohistochemical staining images for osteopontin (OPN) after different treatments. Scale bars: 50 μm.

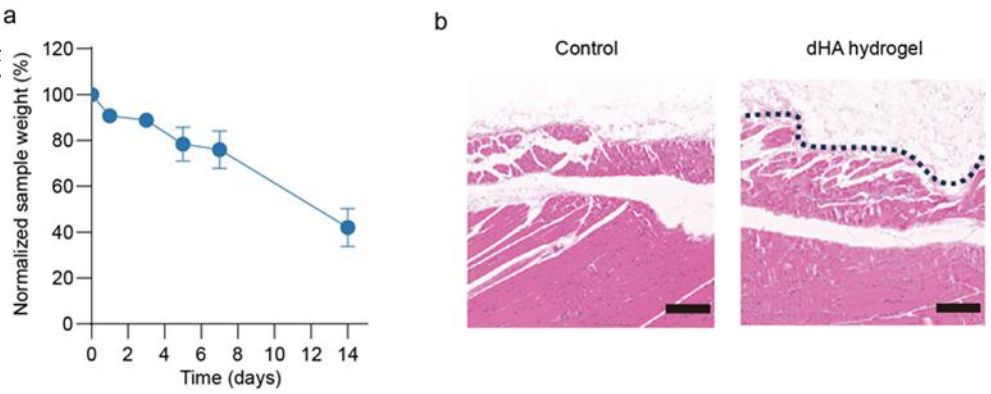

Figure S24. ***In vivo*** **degradation and local biocompatibility of the dHA hydrogel.** (a) Quantification of the residual hydrogel mass, n = 3. All data were expressed as the mean ± SD. The hydrogel mass at day 0 was normalized to 100%. (b) Representative H&E staining of subcutaneous tissue of hydrogel implantation site. Scale bars: 100 μm. The dashed lines indicate the hydrogel region.

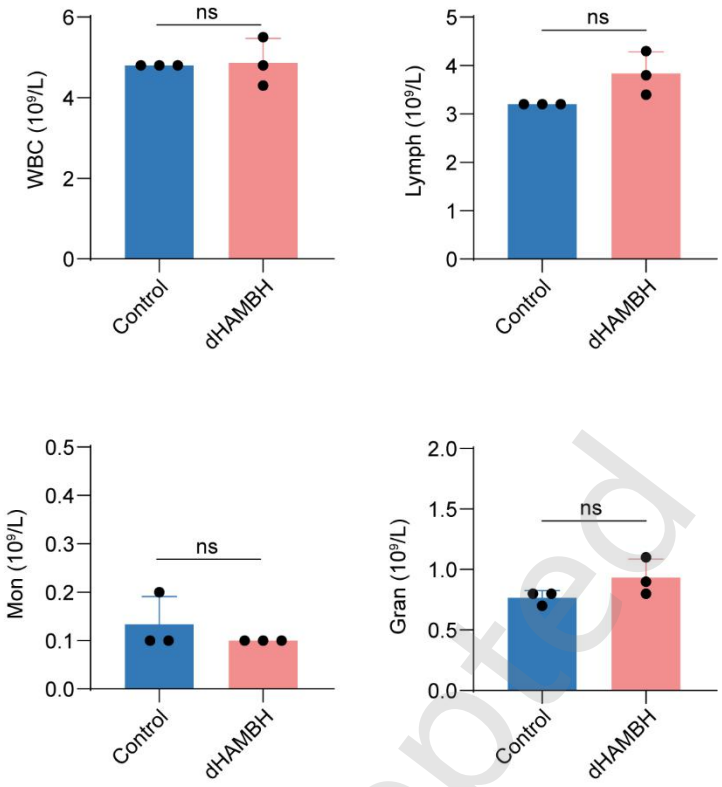

Figure S25 Complete blood panel analysis of white blood cells (WBC), lymphocytes (Lymph), monocytes (Mon), and neutrophils (Gran) in dHAMBH-treated and PBS-treated groups at 14 days post-treatment, n =3. All data were expressed as the mean ± SD.

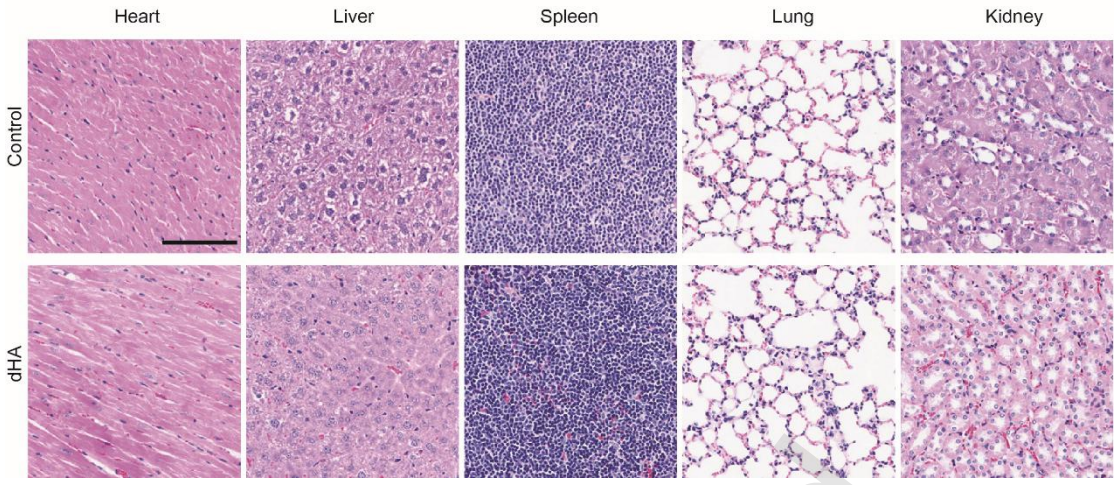

Figure S26 Histological analysis of major organs (heart, liver, spleen, lung, and kidney) from dHAMBH-treated and PBS-treated groups at 14 days post-treatment. Scale bar: 100 μm.